EXPERIMENTAL AND NUMERICAL INVESTIGATION OF CRYSTALLIZATION KINETICS IN SELECTIVE LASER SINTERING

RESEARCH AND DEVELOPMENT PROJECT

FREDERIK BOJE MUNK,

JESPER HESSELVIG,

RASMUS THOFT NYGAARD,

PROJECT REPORT

February 2026

Supervisor: Michael Sandberg

AARHUS
UNIVERSITY

DEPARTMENT OF MECHANICAL AND PRODUCTION ENGINEERING

EXPERIMENTAL AND NUMERICAL INVESTIGATION OF CRYSTALLIZATION KINETICS IN SELECTIVE LASER SINTERING

Research and Development Project

FREDERIK MUNK, JESPER HESSELVIG & RASMUS NYGAARD

Project Report

Department of Mechanical and Production Engineering
Faculty of Technical Sciences
Aarhus University

February 2026

Abstract

The selective laser sintering process depends on tight coupling between thermal history and polymer crystallization to achieve parts with good mechanical properties. This study experimentally examines crystallization of carbon fiber reinforced polyamide 11 during selective laser sintering. Differential scanning calorimetry is used to experimentally characterize crystallization kinetics under isothermal and non isothermal conditions. The kinetics are coupled with a numerical print scale thermal model.

Results show strong sensitivity of relative crystallinity to temperature and cooling history. Crystallization exhibits both primary and secondary mechanisms, with slower secondary crystallization becoming dominant at later stages of crystallization. A Dual Nakamura formulation is chosen to represent primary and secondary crystallization and is fitted to experimental data. The model shows good agreement with independent non-isothermal measurements at low cooling rates.

Numerical simulations resolve temperature fields and relative crystallinity during printing and cooling. Thermal gradients and cooling rates drive spatial variation of crystallization across the build volume. The combined experiments and simulations can guide process parameter selection and part placement to improve consistency and mechanical performance.

Frederik Munk, Jesper Hesselvig & Rasmus Nygaard: *Experimental and Numerical Investigation of Crystallization Kinetics in Selective Laser Sintering,* Project Report © February 2026

CONTENTS

Acknowledgements

This project would not have been possible without the assistance of Carsten Bloch. He introduced us to the relevant laboratory equipment, arranged the procurement of the equipment required for the project, and provided valuable guidance in assessing and interpreting the results of the laboratory work.

1 INTRODUCTION

1.1 Additive manufacturing

Additive manufacturing (AM) is a modern production technique that builds three-dimensional objects layer by layer from digital designs, rather than shaping or cutting material from a solid block. AM technologies originated in the 1980s to support rapid prototyping: producing models, concept parts or functional mock-ups quickly for design verification rather than full production manufacture. [13] With the development of AM technologies, it can now be used for small-scale series production of functional end-use components. This shift from prototyping to production has been driven by the development of more advanced AM processes. One such process, Selective Laser Sintering (SLS), has gained significant industrial adoption due to its versatility and material efficiency. [48], [**1.1**, 22]

1.1.1 Selective Laser Sintering

Selective Laser Sintering is one of the most established powder-bed fusion techniques within additive manufacturing. As illustrated in Figure 1.1, the printer works by gradually spreading a thin layer of polymer powder across the heated build platform using a powder roller. A laser beam scans the cross-sectional geometry of the part, sintering the powder particles into a solid structure. Once one layer is completed, the build platform lowers, and a new layer of powder is deposited from the powder stock onto the print bed by the powder roller. This cycle is repeated iteratively, until the full three-dimensional geometry is formed. The process builds the part directly from a CAD model, without requiring molds or support structures. [23]

The choice of powder material strongly influences the mechanical and thermal performance of SLS parts. Early implementations primarily used unfilled aliphatic polyamides, valued for their good sintering behavior, low moisture absorption and isotropic mechanical properties. In recent years, the industry has increasingly explored the incorporation of various reinforcements into polymer powders, such as carbon fibers, glass beads, and

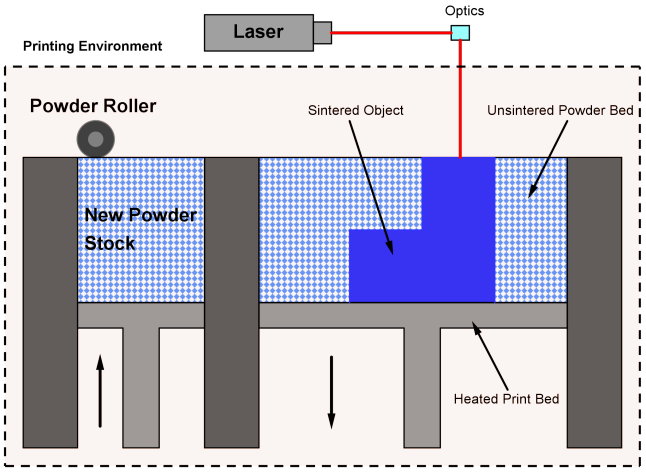

Figure 1.1: Illustration of SLS-printing process [1],[17]

aluminum particles. These additives are intended to enhance the stiffness, strength, thermal stability, and overall performance of the final parts, further expanding the applicability of SLS. [14], [49] Among the aliphatic polyamides used in SLS, carbon reinforced PA11 is one of the strongest and most versatile materials available on the powder market. [49]

1.1.2 PA11-CF

PA11 is a semi crystalline thermoplastic known for its mechanical properties, chemical resistance, and dimensional stability. [24] Being composed of primarily linear polymer chains, it can achieve a high degree of crystallization after sintering, a factor that enhances its mechanical performance. [10]

The addition of carbon fibers further improves the material properties. SLS parts produced with carbon fiber reinforced PA11 are capable of fulfilling demanding structural requirements in engineering applications. The carbon fiber reinforcement specifically increases tensile and flexural strength, enhances stiffness, and improves thermal stability, while also reducing part deformation and improving corrosion resistance. The magnitude of these benefits depends on fiber content, length and dispersion, as well as the chosen process parameters. [46]

The main advantage of semicrystalline polymers in SLS printing comes from sharp melting behavior. When the processing temperature exceeds the melting temperature, the crystalline structure disappears over a narrow temperature range. The ordered lamellae structure break down and the polymer becomes an amorphous melt. During cooling, polymer chains reorganize and recrystallize. The ordered molecular arrangement and intermolecular interactions within crystalline regions enhance stiffness and strength. During SLS, the cooling process influences the degree of crystallinity. Therefore, achieving the desired mechanical properties in the final part requires a thorough understanding of crystallization kinetics during SLS process. [6]

1.2 Approach

This study investigates crystallization kinetics in selective laser sintering of PA11-CF by combining experiments and numerical modeling. Differential scanning calorimetry is used to characterize crystallization behavior under both isothermal and non-isothermal conditions. A crystallization kinetics model is integrated with a print-scale thermal simulation to predict temperature evolution and relative crystallinity throughout the SLS process and subsequent cooling. This work provides a coupled experimental and modeling framework linking process conditions to thermal history and crystallinity development. These insights can guide process optimization and improve material performance in SLS.

2 THEORY

This chapter presents the theoretical framework for modeling polymer crystallization and heat transfer during selective laser sintering. It covers the structure and behavior of semi-crystalline polymers, the kinetics of crystallization under isothermal and non-isothermal conditions, and the coupling of crystallization with heat transfer.

2.1 Crystallinity in Polymers

Polymer crystallinity describes the ordered atomic array of molecule chains within a polymer. Crystalline regions in polymers form when molecular chains align and pack in a regular, repeating pattern. Any chain disorder or misalignment leads to amorphous regions within the material. Due to the large size and complex structure of polymer molecules amorphous regions are unavoidable and polymers only become partially crystalline, also referred to as semicrystalline. [10, 40].

2.1.1 Semi-crystalline Polymers

A semi-crystalline polymer consists of crystalline regions dispersed within the amorphous phase, as illustrated in Figure 2.1.

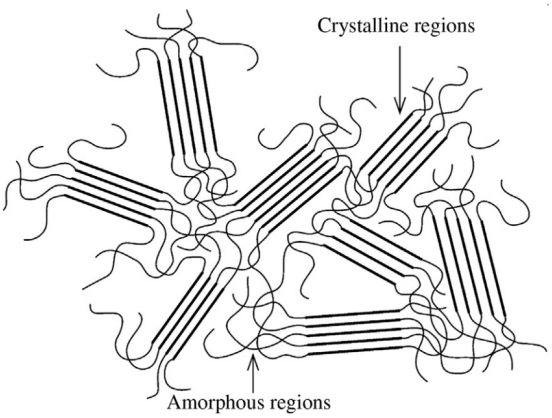

Figure 2.1: Amorphous and crystalline regions in a semi-crystalline polymer. Taken from [29]

In polymers such as PA11, crystalline regions form from the melt during cooling. Linear polymers, like PA11, crystallize more readily than branched, network, or crosslinked polymers. In such structures, branches hinder chain alignment and reduce the formation of crystalline regions. [10] In SLS, the polymer powder transitions from a solid to a molten phase as it absorbs heat from the laser. [47] Primary nucleation occurs during cooling, when sites in the melt initiate

crystal formation. This happens as entangled amorphous chains fold and stack into an ordered lamellae structure. Once crystal structures appear, secondary nucleation begins, serving as a crystal perfectioning process involving lamellar thickening and chain reorganization. [39] This leads to the formation of thin lamellar structures arranged in multilayered formations known as crystallites. The extent of crystallization depends on the cooling rate, since molecular chains require sufficient time and mobility to align properly. [10, 40] During crystallization energy is released; as such it is an exothermic process. This released energy is referred to as the crystallization enthalpy. During re-melting, the crystal formation is broken down and the energy needed for this process will equal the crystallization enthalpy in magnitude. From this, the crystallinity of a material can be found by determining the crystallization enthalpy during melting. [37]

The crystallites grow radially from the nucleation sites, forming a spherulite structure that contains both amorphous and crystalline regions; see Figure 2.2. These spherulite structures are polymer analogs of grains in metals and ceramics. [10, 40]

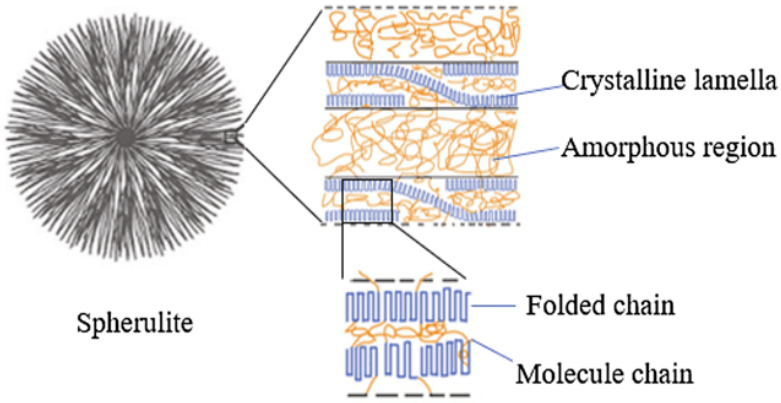

Figure 2.2: Schematic representation of polymer spherulite. Taken from [45]

The superior mechanical performance of semi-crystalline polymers is a result of the van der Waals bondings between chains. While these secondary forces are weaker than covalent bonds, the high degree of chain alignment within crystalline regions enhances intermolecular attraction, thereby increasing stiffness. Moreover, the overall degree of crystallinity contributes to interchain bonding between crystalline domains, further strengthening the material. However, a higher crystallinity level, while improving strength and stiffness, also reduces ductility, making the polymer more brittle. [10]

2.2 Crystallinity Kinetics

Crystallinity kinetics is commonly modeled with temperature as the dominant controlling parameter. [3, 10] An important reference regarding the temperature is the equilibrium melting temperature, T_m°, defined as the melting point of crystals large enough that surface effects are negligible. At T_m°, crystals are in thermodynamic equilibrium with the surrounding melt,

representing the melting point of ideal, defect-free crystals. [18] Keeping this in mind, different models for describing both isothermal- and non-isothermal crystallization can be discussed.

2.2.1 Isothermal Crystallization

For isothermal crystallization of PA11, the Avrami equation can be applied to describe the crystallinity kinetics. [28] The Avrami model was originally developed for metals, but has been adopted for polymers. During isothermal crystallization, crystal formation begins slowly, accelerates, and then gradually declines as the process nears completion. This behavior produces a sigmoidal-shaped transformation curve. [3]

The theoretical description of this behavior is based on a set of assumptions supported by experimental observations. Crystallization starts from nucleiation sites, $\overline{N}$, in the melt. The number of active nuclei, $N(t)$, decreases over time in two ways. First, nuclei become growth centers with probability $\nu(t)$. Secondly, they are consumed by growing spherulites, whose volume is determined by the linear growth rate $\dot{G}$ and shape σ of the spherulite. [4]

These observations are modeled using the Avrami equation expressed in [3–5]:

$$\alpha_{cry}(t) = 1 - \exp(-kt^n) \tag{2.1}$$

Here, $\alpha_{cry}(t)$ is the relative crystallinity. It should be noted that even when the phase transformation is complete ($\alpha_{cry} = 1$), the absolute crystallinity χ is less than one, since no polymer is completely crystalline. [10]

The exponent, n, known as the Avrami exponent, describes the dimensionality of crystal growth. $n = 1$ corresponds to one-dimensional growth, while $n = 3$ represents three-dimensional polyhedral growth. [5] In recent studies, n is often treated as a fitting parameter that governs the steepness of the transformation curve. The constant k is a composite rate constant, controlling the overall transformation rate with proportionality $k \propto \sigma, \dot{G}, \overline{N}, \nu$. A higher k value indicates faster crystallization.

For polymers, the composite rate constant $k(T)$ is defined based on the crystallization half-time $t_{1/2}$. [28] The crystallization half-time is the time required for the phase transformation to reach $\alpha = 1/2$ at a specified annealing temperature. Substituting this condition into Eq. (2.1) and isolating $k(T)$ yields:

$$k(T) = \frac{\ln(2)}{t_{1/2}^n} = \ln(2) R_C(T)^n \tag{2.2}$$

The crystallization rate $R_C = {t_{1/2}}^{-1}$ is determined using the Lauritzen-Hoffman equation [26]:

$$R_C(T) = R_0 \exp\left(-\frac{U}{R(T - T_\infty)}\right) \exp\left(-\frac{K_g}{T\Delta T f}\right) \tag{2.3}$$

R_0 is a pre-exponential factor representing the maximum possible crystallization rate, U is the material-specific activation energy for crystallization, and $R = 8.314\,\mathrm{J/(mol \cdot K)}$ is the universal

gas constant. The first exponential term accounts for the retardation of crystallization as the temperature approaches a reference temperature,$T_\infty = T_g - 30$ K, where T_g denotes the glass transition temperature. At T_∞, molecular chains become immobile and crystallization ceases. [26] Therefore, the equation is not valid for temperatures below T_∞, as it is assumed that no crystallization occurs below this point.

The second exponential term represents the surface nucleation rate, i.e., the rate at which new lamellar structures form on existing nuclei. K_g is an experimentally determined nucleation parameter related to the polymer's surface free energies, describing the difficulty of adding new layers to the crystallite. The degree of supercooling is defined as $\Delta T = T_m^\circ - T$. As ΔT increases, the nuclei become more stable due to reduced thermal atomic vibrations, which otherwise disrupt the ordered molecular arrangements and weaken intermolecular forces. Therefore, the equation is not valid for temperatures above T_m°, since no crystalline structures can form beyond this point. The factor f is a correction term that accounts for changes in the heat of fusion with temperature. [26]

$$f = \frac{2T}{T_m^\circ + T} \tag{2.4}$$

2.2.2 Non-Isothermal Crystallization

To describe non-isothermal crystallization kinetics, Nakamura [32, 33] proposed that the process can be represented as a sequence of infinitesimal isothermal steps. The non-isothermal crystallization behavior can be expressed in a form analogous to the Avrami equation for isothermal crystallization (Eq. (2.1)):

$$\alpha_{cry} = 1 - \exp\left[-\left(\int_0^t K(T(t))\, d\tau\right)^n\right] \tag{2.5}$$

Assuming Eq. (2.5) is identical to the Avrami equation (Eq. (2.1)) at each infinitesimal isothermal step, the effective rate constant for non-isothermal crystallization, $K(T)$, can be related to the isothermal rate constant $k(T)$ from Eq. (2.2) through the following relation [32]:

$$K(T) = k(T)^{\frac{1}{n}} = \ln(2)^{\frac{1}{n}} R_C(T) \tag{2.6}$$

where n is the Avrami exponent.

2.2.3 Dual Nakamura Model and the Effect of Secondary Crystallization

The conventional Nakamura and Avrami models often neglect the slower kinetics associated with secondary crystallization, which leads to an overprediction of the relative crystallinity at the end of the phase transformation. At the start of the phase transformation, primary crystallization dominates, as nuclei grow without significant interference. As growth progresses, the structures begin to interfere with neighboring regions, restricting growth. At this point, the slower secondary crystallization becomes the dominant mechanism. [39]

Velisaris and Seferis, [44], proposed a dual modelling approach to describe the effect of secondary crystallization, given by:

$$\alpha_{cry} = P_p \left[1 - \exp\left(-\left(\int_0^t K_p(T(t))\, d\tau\right)^{n_p}\right)\right] + P_s \left[1 - \exp\left(-\left(\int_0^t K_s(T(t))\, d\tau\right)^{n_s}\right)\right], \quad (2.7)$$

where the subscripts p and s denote the primary and secondary crystallization processes, respectively.

This formulation was further developed by Seo et al. [39], who proposed that the weight factors P_p and P_s depend on the relative crystallization, such that $P_p = 1 - \alpha_{cry}$ and $P_s = \alpha_{cry}$. This leads to the following relation:

$$\alpha_{cry}(t) = \frac{1 - \exp\left[-\left(\int_0^t K_p(T(t))\, d\tau\right)^{n_p}\right]}{1 - \exp\left[-\left(\int_0^t K_p(T(t))\, d\tau\right)^{n_p}\right] + \exp\left[-\left(\int_0^t K_s(T(t))\, d\tau\right)^{n_s}\right]} \quad (2.8)$$

The effective rate constants for non-isothermal crystallization of the primary and secondary processes can be determined using Eq. (2.6):

$$K_p(T) = [\ln(2)]^{\frac{1}{n_p}} R_C(T) \quad (2.9)$$

$$K_s(T) = [\ln(2)]^{\frac{1}{n_s}} R_C(T) \quad (2.10)$$

With the theoretical framework for modeling non-isothermal crystallization kinetics established, an equally important aspect is coupling the crystallization kinetics with heat transfer. Crystallization kinetics is dependent on heat transfer and the crystallization process itself affects the heat transfer since it is an exothermic process.

2.3 Heat Transfer with Crystallization Coupling

The purpose of the thermal coupling is to integrate the crystallization model into a heat transfer framework for SLS printing. The goal is to present a numerical model that resolves heat transfer and crystallization kinetics at the same time during the SLS process. This is done by using the print-scale heat transfer model developed in [43], where the material parameters are adjusted to represent PA11-CF.

The heat transfer is described by the general heat conduction equation [50]:

$$\rho c_p \frac{\partial T}{\partial t} + \nabla \cdot (-k \nabla T) = \dot{q} \quad (2.11)$$

Here, ρ is the density [kg/m^3], c_p is the specific heat capacity [J/(kg $\cdot$ K)], k is the thermal conductivity [W/(m $\cdot$ K)], and $\dot{q}$ is the internal heat generation per unit volume [W/m^3].

2.3.1 Addition of Layers

To model the addition layers in the SLS process. The continuous approach proposed in [43] is adopted for its high numerical efficiency. In this method, the entire geometry, is treated as a single computational domain. Layers that are not yet active are assigned a very low thermal conductivity, k, effectively suppressing heat transfer between active and inactive regions.

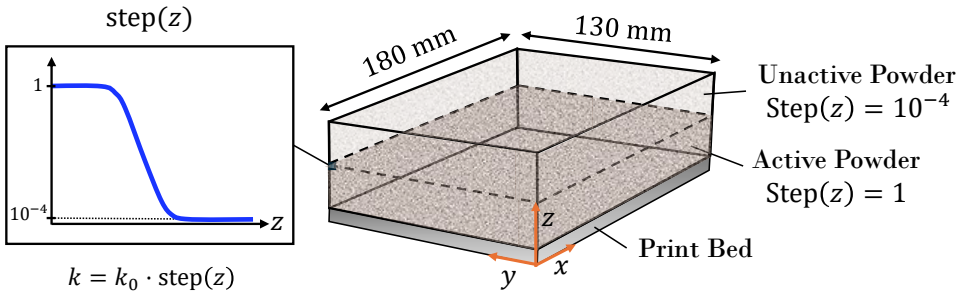

Figure 2.3: Illustration of layer addition. Taken from [43]

This behavior is governed by a vertical step function, which smoothly transitions between active and inactive layers (see Figure 2.3), and is defined as:

$$\text{step}(z) = 1 - \left(\frac{1}{2} \left[1 + \tanh\left(\frac{z - z_c}{\frac{n_{\text{layer}} h_{\text{layer}}}{2}} \right) \right] \left(1 - 10^{-4} \right) \right), \tag{2.12}$$

Here, h_{layer} denotes the height of a single physical powder layer, and n_{layer} is the number of physical layers grouped into a single computational layer. Increasing $n_{\text{layer}} > 1$ enhances computational efficiency but leads to a reduction in spatial accuracy. The position of the transition zone is controlled by the parameter z_c, which evolves over time according to

$$z_c(t) = v_z t + z_0, \tag{2.13}$$

where v_z is the vertical build rate of the printer and z_0 is the initial height at the onset of the printing process.

2.3.2 Laser Source Model

Following [43], the volumetric laser heat source is expressed as:

$$\dot{q}_{\text{laser},V}(z,t) = \dot{q}_0 \, f(z,t), \tag{2.14}$$

where the function $f(z,t)$ describes the temporal and vertical distribution of the laser power. For numerical efficiency, a unit Gaussian profile is employed, as proposed in [43], given by

$$f(z,t) = \frac{1}{\sigma\sqrt{2\pi}} \exp\left[-\frac{1}{2} \left(\frac{z - v_z t}{\sigma} \right)^2 \right]. \tag{2.15}$$

Here, σ represents the standard deviation of the Gaussian distribution. Larger values of σ result in broader and flatter profiles, while smaller values yield narrower and more localized heat distributions. The center of the Gaussian moves upward at the vertical build rate v_z.

In this work, σ is taken as the attenuation length γ, which describes the depth over which the laser intensity decreases to $1/e$ of its value at the surface. [34]

The laser heat source intensity $\dot{q}_0$ is chosen such that the temporal integral of the heat source yields the volumetric energy density, resulting in

$$E_v = \dot{q}_0 \int_{-\infty}^{\infty} f(z,t)\, dt = \frac{\dot{q}_0}{v_z}. \tag{2.16}$$

The volumetric energy density is defined in [43] as:

$$E_v = \frac{K P_0}{v_{\text{laser}}\, h_{\text{hatch}}\, h_{\text{layer}}}, \tag{2.17}$$

Isolating $\dot{q}_0$ from Eq. (2.16) gives

$$\dot{q}_0 = E_v\, v_z = \frac{P_0\, K\, v_z}{v_{\text{laser}}\, h_{\text{hatch}}\, h_{\text{layer}}}. \tag{2.18}$$

In this expression, P_0 denotes the laser power [W], v_{laser} is the laser scanning speed [m/s], h_{hatch} represents the hatch spacing [m], and h_{layer} is the layer thickness [m]. The absorption coefficient, K, corresponds to the fraction of the laser energy absorbed by the material.

2.3.3 Initial and Boundary Conditions

Following the approach in [43], newly added layers are assumed to be at a high temperature near the polymer melting point, and their temperature is considered uniform throughout. The initial condition is therefore prescribed as

$$T(x,y,z,0) = T_0. \tag{2.19}$$

Since the top surface between the active and inactive layers moves during the process, the method from [43] is adopted, in which convective and radiative losses at the top boundary are modeled using a heat sink approach:

$$\dot{q}_{\text{conv,V}} = h_{\text{air}}\,(T_{\text{air}} - T)\cdot f(z,t), \tag{2.20}$$

$$\dot{q}_{\text{rad,V}} = \epsilon\sigma_B \left(T_{\text{air}}^4 - T^4\right)\cdot f(z,t), \tag{2.21}$$

where $f(z,t)$ is defined in Eq. (2.15). These terms are added to the volumetric heat generation term in Eq. (2.11), together with the laser heat source Eq. (2.14), yielding

$$\rho c_p \frac{\partial T}{\partial t} + \nabla\cdot(-k\nabla T) = \dot{q}_{\text{laser},V} + \dot{q}_{\text{conv,V}} + \dot{q}_{\text{rad,V}}. \tag{2.22}$$

For the sides and bottom of the build platform, heat losses are modeled using an equivalent convective flux, following the method in [27].

$$\dot{q}_{\text{side}} = -\vec{n}_{\text{side}} \cdot (k\nabla T) = -h_{\text{side}} \left(T - T_{\text{side}}\right). \tag{2.23}$$

During the cooling stage, the entire geometry is built, and the powder bed gradually cools to room temperature. Radiation and convective losses to the environment are assumed to occur at the top surface:

$$\dot{q}_{\text{top, cool}} = -\vec{n}_{\text{top}} \cdot (k\nabla T) = -h_{\text{air}} \left(T - T_{\text{air,cool}}\right) - \sigma_B \varepsilon \left(T^4 - T_{\text{air,cool}}^4\right), \tag{2.24}$$

where $T_{\text{air,cool}}$ [K] is the ambient temperature during cooling. For the side and bottom boundaries in Eq. (2.23), the build platform temperature is assumed to follow a prescribed cooling program, $T_{\text{side}} = T_{\text{side,cool}}$.

The cooling is assumed linear from the print temperatures T_{air} and T_{side} to room temperature and is modeled as:

$$T_{\text{cool}} = \begin{cases} T_{\text{air}}/T_{\text{side}}, & t \leq t_{\text{cooling,start}} \\ -\frac{T_{\text{air}}/T_{\text{side}} - 20\,^\circ\text{C}}{\Delta t_{\text{cool}} \cdot (t - t_{\text{cooling,start}})} + T_{\text{air}}/T_{\text{side}} & t_{\text{cooling,start}} < t < t_{\text{cooling,start}} + \Delta t_{\text{cool}} \\ 20\,^\circ\text{C}, & t \geq t_{\text{cooling,start}} + \Delta t_{\text{cool}} \end{cases} \tag{2.25}$$

Here, $t_{\text{cooling,start}}$ denotes the time when the print process ends and cooling begins, and Δt_{cool} controls the rate of cooling to room temperature.

2.3.4 Phase Change and Crystallization Coupling

To describe phase changes during melting, a step function is used following the approach in [42, 43], where it is assumed that the melt kinetics are not sensitive to the heating rate:

$$\alpha_{melt}(T) = \frac{1}{2} \left(\tanh\left(b\left(T - T_m\right)\right) + 1\right). \tag{2.26}$$

Here, T_m is the melting point, and b determines the width of the phase transition, with higher values producing sharper transitions. The function is defined such that $\alpha_{melt}(T) = 0$ corresponds to the solid state, while $\alpha_{melt}(T) = 1$ corresponds to the fully melted state. During melting, the material transitions from a powder to a solid, leading to an increase in density. Following the approach in [43], this change is described as:

$$\rho(T_{\text{max}}) = \rho_{\text{bulk}} + (\rho_{\text{solid}} - \rho_{\text{bulk}}) \cdot \alpha_{melt}(T_{\text{max}}), \tag{2.27}$$

where T_{max} is the maximum temperature reached during sintering. Details on how to obtain this are provided in Section 3.4.1. Using the maximum temperature, ensures that the material does not revert to a powder upon cooling.

For the thermal conductivity, a volume-averaging approach based on porosity is applied [16]:

$$k_{\text{powder}}(\rho, z) = k_{\text{solid}}\,(1 - \phi(\rho)) \cdot \text{step}(z), \tag{2.28}$$

where the porosity is defined as

$$\phi(\rho) = \frac{\rho_{\text{solid}} - \rho}{\rho_{\text{solid}}}. \tag{2.29}$$

To account for crystallization, the heat released during the process is included as an internal heat source, following the approach in [42]:

$$\rho c_p \frac{\partial T}{\partial t} + \nabla \cdot (-k \nabla T) = \dot{q}_{\text{laser},V} + \dot{q}_{\text{conv,V}} + \dot{q}_{\text{rad,V}} + \dot{\alpha}_{cry}\,\rho\,\Delta H_{\infty,cry} \tag{2.30}$$

where $\Delta H_{\infty,cry}$ represents the latent heat of crystallization. A constant $\Delta H_{\infty,cry}$ is assumed following the approach in [42]. However, the degree of crystallinity depends on the cooling rate, with slower cooling leading to higher crystallinity. [10] The validity of this assumption will be further discussed in Section 4.1.4.

The effective specific heat capacity is given by

$$c_p = c_{p,0} + \text{HorC} \cdot \frac{d}{dT}\alpha_{melt}(T) \cdot \Delta H_{\infty,\text{melt}}, \tag{2.31}$$

where $c_{p,0}$ is the base specific heat outside the phase transformation, assumed to be constant. This assumption will be further discussed in Section 4.1.1. The term '$\frac{d}{dT}\alpha_{melt}(T) \cdot \Delta H_{\infty,\text{melt}}$' accounts for the heat absorbed during melting, while the heat released during crystallization is included in Eq. (2.30) as a source term. The variable HorC indicates whether the material is heating or cooling and is used to model the thermal hysteresis of the powder; this variable will be discussed further in Section 3.4.1. Finally, $\Delta H_{\infty,\text{melt}}$ defined the latent heat of melting.

For the degree of phase transformation, the material initially starts as solid, and α_{cry} decreases as melting progresses. Following [42], Eq. (2.26) is modified to describe the relative crystallinity decreasing from 1 to 0 during melting:

$$\alpha_{0,cry}(T_{\max}) = 1 - \alpha_{melt}(T_{\max}). \tag{2.32}$$

Once heating is completed, $\alpha_{0,cry}$ is used as the initial condition for the Dual Nakamura model, Eq. (2.8):

$$\alpha(t) = \frac{1-(1-\alpha_{0,cry}(T_{\max}))\exp\left[-\left(\int_0^t K_p(T(t))\,d\tau\right)^{n_p}\right]}{1-(1-\alpha_{0,cry}(T_{\max}))\exp\left[-\left(\int_0^t K_p(T(t))\,d\tau\right)^{n_p}\right]+(1-\alpha_{0,cry}(T_{\max}))\exp\left[-\left(\int_0^t K_s(T(t))\,d\tau\right)^{n_s}\right]} \tag{2.33}$$

Here, $T_{\max}$ ensures that the initial condition does not change once cooling begins.

3 METHODS

This section presents the implementation of the crystallization kinetics of PA11-CF within a print-scale SLS model. The experimental procedures conducted to determine the material-specific parameters of PA11-CF are outlined. Using these experimentally derived parameters, the subsequent integration of the theoretical framework introduced in Chapter 2 into the print-scale SLS model will then be detailed. In-detail experiment reports outlining the experimental setups, procedures, and results for all experiments have been attached in the "Experimental Reports" - folder.

3.1 Experimental Approach

This study employed an experimental approach to collect data on isothermal and non-isothermal crystallization, specific heat capacity, first latent heat of melting, and latent heat of crystallization. Isothermal crystallization data were used to model the primary Avrami exponent and crystallization half-time. Non-isothermal crystallization data were used to fit the parameters R_0, U, K_g and n_s in the Dual Nakamura model. The calibrated Dual Nakamura model was subsequently coupled with an existing thermal model to obtain a combined thermal–crystallization model for PA11-CF.

3.2 Differential Scanning Calorimetry

Differential scanning calorimetry (DSC) is employed to characterize the thermal behavior and crystallization kinetics of PA11-CF powder. The results provide key thermal parameters required for a coupled print-scale thermal and a crystallization kinetics model of the SLS process. Four DSC experiments were conducted to evaluate specific heat capacity, isothermal crystallization, non-isothermal crystallization, print location effect on degree of crystallization, first latent heat of melting and latent heat of crystallization for PA11-CF.

For the experiments, a DSC heat flux cell was used, as shown schematically in Figure 3.1. In DSC the heat flow of a material sample during a controlled heating or cooling is measured. The instrument determines the heat flow of the sample by measuring the difference in heat flow between the sample and an empty reference pan placed inside the measuring cell. [36] A purge gas is applied to maintain an inert and dry atmosphere inside the measurement cell, ensuring reproducible results. [2] Outside the measurement cell, a protective gas is used to extend the lifetime of the cell without affecting the experimental results. [12]

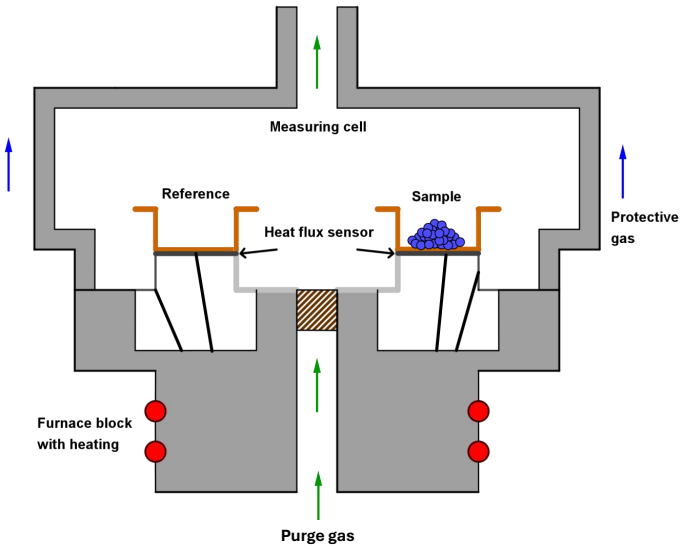

Figure 3.1: Schematic of DSC cell. Taken from [17]

The DSC 3 Thermal Analysis System from METTLER TOLEDO is used for the experiments. The system uses nitrogen both as purge and protective gas. The STARe Evolution software was used for extracting data and creating thermal programs [30], while post-processing was carried out in MATLAB. The analysis was done for virgin PA11 carbon fiber-reinforced powder (virgin PA11-CF). The term *virgin* refers to powder that has not been previously handled and comes directly from the factory.

The methodology applied in this work follows the general principles of differential scanning calorimetry as described in DS/EN ISO 11357-1:2023. [21] The determination of specific heat capacity and the evaluation of crystallization and melting behavior are conducted in accordance with DIN EN ISO 11357-4:2021 [19] and DS/EN ISO 11357-7:2022 [20], respectively.

All DSC measurements are assumed to occur at constant pressure, allowing the sample's heat flow to be expressed as:

$$\frac{\dot{Q}}{m} = c_{p,0}(T)\dot{T} + \dot{\alpha}\Delta H_{\infty} \tag{3.1}$$

Where $\dot{Q}$ is the heat flow [W], m is the sample mass [kg], $c_{p,0}(T)$ is the base specific heat capacity at constant pressure [J/(kg · K)], $\dot{T}$ is the heating rate [K/s], $\dot{\alpha}$ is the degree of phase transformation rate [1/s] and ΔH_{∞} is the latent heat associated with the phase transition [J/kg]. In Eq. (3.1), the DSC heat flow represents a combination of contributions from both the base specific heat capacity $c_{p,0}(T)$ and the phase transition. This is illustrated in Figure 3.2.

The latent heat associated with the phase transformation is obtained by integrating the difference between the measured heat flow per unit mass, $\frac{\dot{Q}(t)}{m}$, and the baseline specific heat contribution, defined by the integration line $\frac{\dot{Q}_{IL}(t)}{m}$, over the phase transition period. [20]

$$\Delta H_{\infty} = \int_{t_0}^{t_{end}} \frac{\dot{Q}(t) - \dot{Q}_{IL}(t)}{m}\, dt \tag{3.2}$$

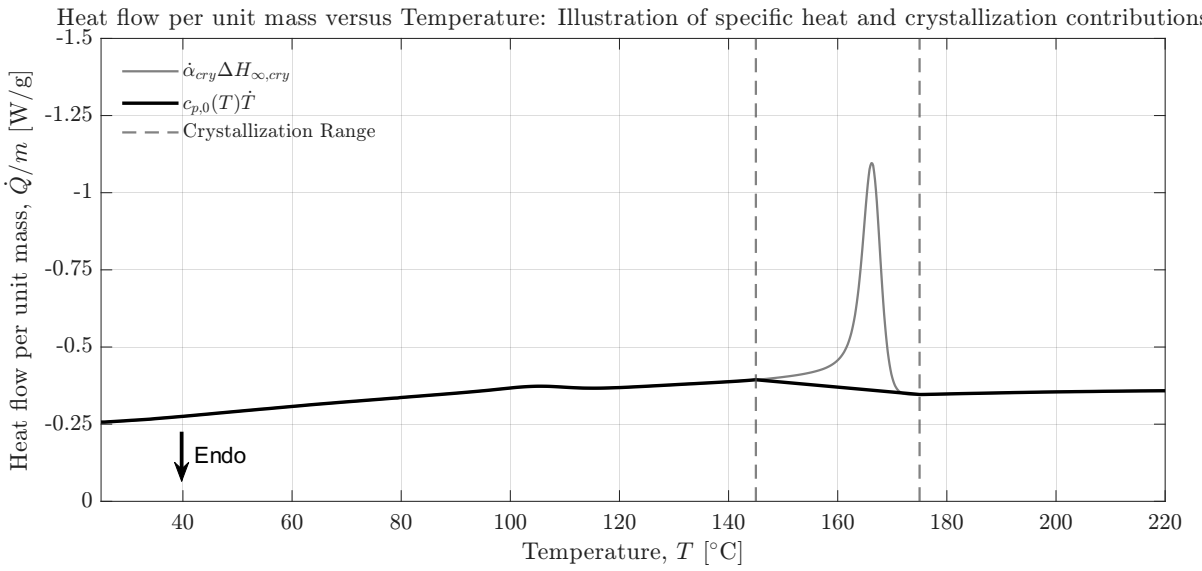

Figure 3.2: Visualization of the heat flow per unit mass contributions from specific heat and crystallization.

$\dot{Q}_{IL}$ [W] is defined as a linear baseline between the start, t_0 [s], and end, t_{end} [s], of the phase transition. In this report, $c_{p,0}$ is modeled as a constant. The method for selecting t_0 and t_{end} varies between experiments and is described in the respective sections. In reality, $c_{p,0}$ should align with the chosen integration lines. More detailed modeling could ensure more precise alignment, but this is beyond the scope of this project.

The phase transition enthalpy change, $\Delta H(t)$, is determined similarly to Eq. (3.2), using a cumulative integral within the phase transition period. [20]

$$\Delta H(t) = \int_{t_0}^{t} \frac{\dot{Q}(\tau) - \dot{Q}_{IL}(\tau)}{m}\, d\tau \tag{3.3}$$

Utilizing Eq. (3.3) and (3.2), the degree of phase transformation can be determined by [20]:

$$\alpha(t) = \frac{\Delta H(t)}{\Delta H_{\infty}} \tag{3.4}$$

When the phase transition of crystallization is being measured, the degree of phase transformation represent the relative crystallinity.

$$\alpha_{cry}(t) = \frac{\Delta H_{\text{cry}}(t)}{\Delta H_{\infty,\text{cry}}} \tag{3.5}$$

3.2.1 Determination of specific heat capacity & first latent heat of melting

To model the thermal response of PA11-CF, the specific heat must be determined. Since the thermal history and possible heat treatment of the factory-supplied PA11-CF are unknown, the first latent heat of melting, $\Delta H_{\infty,\text{melt}}$, from Eq. (2.31), also needs to be experimentally

characterized using DSC. The calculations and data processing were performed using the attached MATLAB files: 'Latent_Heat_Melting.m' & 'cp_Determined.m'.

DSC measurements were performed on three different samples, and the specific heat was taken as the average of the three runs. Instrumental baseline runs $\dot{Q}^B(T)$ were conducted between each test and subtracted from the sample run $\dot{Q}^S(T)$ to correct for discrepancies between the DSC's sample and reference cells.

$$\dot{Q}(T) = \dot{Q}^S(T) - \dot{Q}^B(T) \tag{3.6}$$

A controlled temperature program was applied, with heating at a rate of $\dot{T} = 10\ \frac{\mathrm{K}}{\mathrm{min}}$ from 25 °C to 240 °C, followed by a hold at 240 °C for 5 min to ensure complete melting. The sample was then cooled to 25 °C at a rate of $\dot{T} = -10\ \frac{\mathrm{K}}{\mathrm{min}}$. A visualization of the thermal program is shown in Figure 3.3.

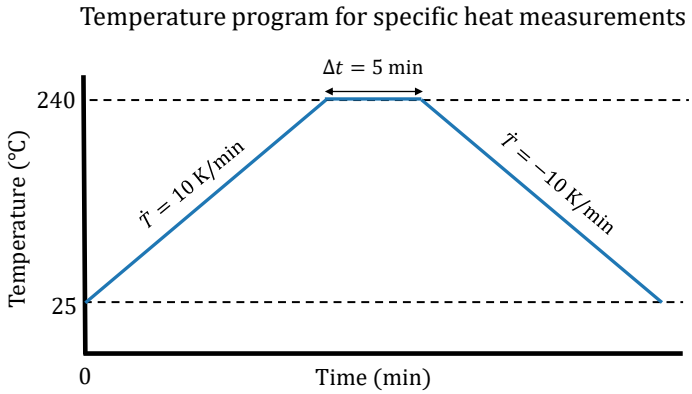

Figure 3.3: Temperature program used for specific heat measurements.

The effective specific heat capacity, including contributions from phase transitions, is given by:

$$c_p(T) = \frac{\dot{Q}(T)}{m \cdot \dot{T}} \tag{3.7}$$

An overview of the samples can be found in Table 3.1.

Experiment No.	Substance	Mass [mg]	Heat rate [K/min]
1	Virgin PA11-CF	9.38	10
2	Virgin PA11-CF	9.23	10
3	Virgin PA11-CF	6.83	10

Table 3.1: Sample overview for c_p measurements.

The first latent heat of melting, $\Delta H_{\infty,\mathrm{melt}}$, was calculated from the averaged heat flow data using Eq. (3.2). The integration line, $\dot{Q}_{IL}$, was manually determined and set between the time indices corresponding to melting start at $T_{ms} = 196°\mathrm{C}$ and the melting end at $T_{mf} = 208°\mathrm{C}$.

3.2.2 Isothermal crystallization

To determine the crystallization half-time, $t_{1/2}$, and the primary Avrami exponent, n_p, the isothermal crystallization behavior of PA11-CF was analyzed. DSC experiments were performed at a range of isothermal temperatures following DS/EN ISO 11357-7:2022. [20]

For each experiment, a sample was heated from 25 °C to 120 °C at 20 $\frac{\text{K}}{\text{min}}$. Samples were then held isothermally for 15 minutes to remove absorbed moisture, following the procedure in [11]. Subsequently, samples were heated at 20 $\frac{\text{K}}{\text{min}}$ to 220 °C and held for 5 minutes to erase prior thermal history. The samples were then cooled as rapidly as possible to the isothermal target temperature, T_{target}. Using the DSC 3 Thermal Analysis System, a maximum cooling rate of 60 $\frac{\text{K}}{\text{min}}$ was possible. T_{target} was held for an annealing time, t_{hold}, that ensured enough time to complete crystallization. A schematic of the thermal program is shown in Figure 3.4.

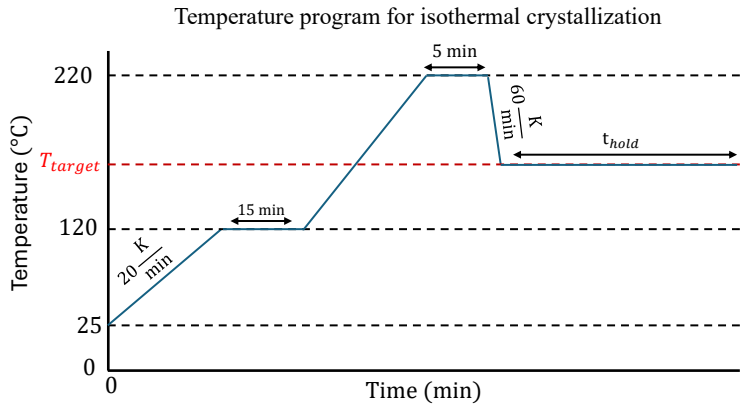

Figure 3.4: Temperature program used for isothermal crystallization measurements.

The experiment was performed at six isothermal target temperatures ranging from 177°C to 182°C in 1°C increments. An overview of the samples tested, sample mass, T_{target} and t_{hold} can be found in Table 3.2

Experiment No.	Substance	Mass [mg]	T_{target} [°C]	t_{hold} [min]
1	Virgin PA11-CF	5.98	177	60
2	Virgin PA11-CF	5.00	178	60
3	Virgin PA11-CF	9.87	179	60
4	Virgin PA11-CF	6.78	180	120
5	Virgin PA11-CF	9.08	181	120
6	Virgin PA11-CF	9.34	182	180

Table 3.2: Sample overview for isothermal crystallization measurements.

The relative crystallinity was calculated using Eq. (3.5). The start and end times of crystallization, t_0 and t_{end}, were manually found as the times where the slope of the heat flow approaches zero. The starting point, t_0, corresponds to the zero-slope region before the crystallization peak, and the end point, t_{end}, corresponds to the zero-slope region after the peak. $t_{1/2}$ is defined as the time at which

$$\alpha_{\text{cry}}(t_{1/2}) = 0.5 \tag{3.8}$$

To determine the primary Avrami exponent, Eq. (2.1) is rewritten to a linear form. In this form n_p represents the slope:

$$\ln\big(-\ln(1-\alpha_{cry}(t))\big) = n_p \ln(t) + k \tag{3.9}$$

Using $\alpha_{\text{cry}}(t)$ measured at different isothermal temperatures, the best-fit slope n_p for all data was obtained using Eq. (3.9). According to [38], primary crystallization is dominant for $\alpha(t) \in [0, 0.25]$. Therefore, n_p was fitted using data in the range $\alpha(t) \in [0.05, 0.25]$. The lower limit of 0.05 is chosen to avoid extreme values in the logarithmic terms of Eq. (3.9) when $\alpha(t) \to 0$.

The methods discussed in this subsection can be seen applied in the attached MATLAB files; 'Isothermal_alpha_time.m', 'T_half.m' and 'Primary_Avrami.m'.

3.2.3 Non isothermal crystallization

To analyze the temperature-dependent crystallization behavior of PA11-CF, non-isothermal experiments were performed.

For the non-isothermal DSC measurements each sample was heated using the same thermal heating program as in Section 3.2.2. After complete melting the material was then cooled to 25 °C at cooling rates varying from 20 $\frac{\text{K}}{\text{min}}$ to 0.2 $\frac{\text{K}}{\text{min}}$. The subsequent temperature programs used for the non-isothermal experiment are shown in Figure 3.5.

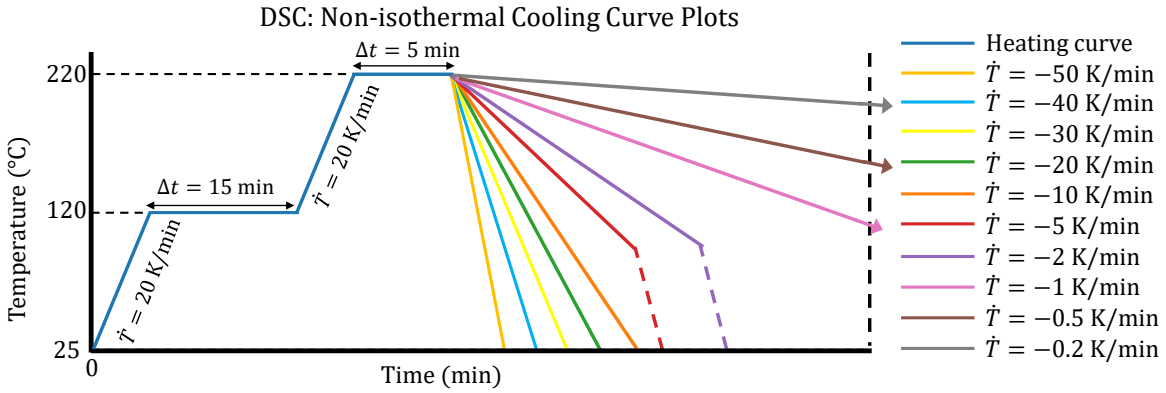

Figure 3.5: Temperature programs used in non-isothermal DSC experiments. For the experiments run at lower cooling rates, they were only run until $T = 140$ °C ($T = 100$ °C for $\dot{T} = -5$ $\frac{\text{K}}{\text{min}}$,$-2$ $\frac{\text{K}}{\text{min}}$), where it was concluded that the samples had reached its end of crystallization.

An overview of the experiments' samples and cooling rates can be found in Table 3.3.

From the heat flow data, the relative crystallinity was calculated using Eq. (3.5). Due to the large number of experiments, in which the start time t_0 and end time t_{end} of crystallization varied, a script was developed to automate the creation of the integration line. The code, the attached MATLAB file; 'LeftRightindexing.m', works by fitting two straight lines to the data well outside the crystallization region on each side of the phase transition, where the heat flow is approximately linear and not influenced by the phase change. The points t_0 and t_{end} are then

Experiment No.	Substance	Mass [mg]	Cooling rate [K/min]
1	Virgin PA11-CF	6.84	50
2	Virgin PA11-CF	9.08	40
3	Virgin PA11-CF	9.02	30
4	Virgin PA11-CF	7.40	20
5	Virgin PA11-CF	9.50	10
6	Virgin PA11-CF	8.20	5
7	Virgin PA11-CF	5.72	2
8	Virgin PA11-CF	9.17	1
9	Virgin PA11-CF	5.84	0.5
10	Virgin PA11-CF	8.30	0.2

Table 3.3: Sample overview for non-isothermal crystallization measurements.

determined by iteratively searching for locations where the fitted line deviates from the actual data beyond a set tolerance.

The methods discussed in this subsection can be seen applied in the attached MATLAB files; 'LeftRightindexing.m' and 'Non_Isothermal_alpha.m'.

3.2.4 Part location effect on degree of crystallinity

DSC measurements of sintered PA11-CF cubes at different positions in the printer were performed to evaluate variations in the degree of crystallinity. The degree of crystallinity is related to the latent heat of crystallization, $\Delta H_{\infty,cry}$, as a higher latent heat indicates a larger fraction of the material has crystallized. In Section 2.3.4, the latent heat of crystallization was assumed to be independent of part position within the printer. This experiment serves to evaluate that assumption and determine the crystallization enthalpy of the sintered material.

It is assumed that the energy released during crystallization, $\Delta H_{\infty,cry}$, is equal to the energy absorbed during re-melting, $\Delta H_{\infty,\text{melt},2}$:

$$\Delta H_{\infty,cry} = \Delta H_{\infty,\text{melt},2} \tag{3.10}$$

For the sintered cubes, the thermal history is assumed to have been erased; therefore, the factory heat treatment to the powder is assumed to have no effect during re-melting of the cubes.

Cubes measuring $15 \times 15 \times 15$ mm were printed in a $5 \times 5 \times 5$ grid, shown in Figure 3.6, using a Sinterit Lisa X SLS printer. Samples were extracted for DSC from the center of the selected cubes. The cubes were chosen along two diagonals, shown in Figure 3.6, through the build volume, ensuring analysis of fully sintered material at different locations within the printer.

Each sample followed the same temperature program shown in Figure 3.7; heating from 25 °C to 240 °C at $5\frac{\text{K}}{\text{min}}$, holding for 5 min to ensure complete melting, and cooling back to 25 °C

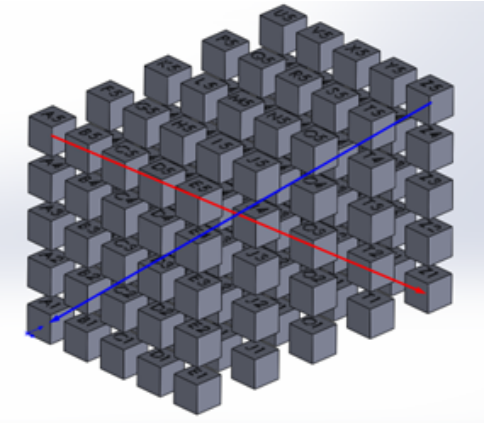

Figure 3.6: Configuration of cubes throughout the print bed with diagonal experiment lines shown in SolidWorks

at $20\frac{\mathrm{K}}{\mathrm{min}}$. The relatively slow heating rate was chosen to promote uniform thermal contact between the crucible and sample.

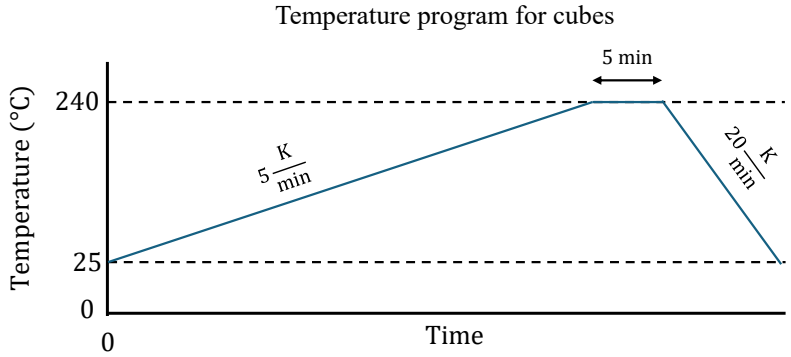

Figure 3.7: Temperature program for experiment on sintered cubes

The mass of the samples, corresponding to the cubes and their distance from the center, was recorded. An overview of the samples can be found in Table **??**.

Experiment No.	Cube name	Mass [mg]	Abs. dist. from center [mm]
1	A5	8.23	98.84
2	G4	8.54	49.42
3	M3	8.80	0.00
4	S2	5.95	49.42
5	Z1	8.72	98.84
6	Z5	7.79	98.84
7	S4	5.99	49.42
8	G2	9.84	49.42
9	A1	6.56	98.84

Table 3.4: Sample overview for cube melting measurements.

From the recorded heat flow signal, $\Delta H_{\infty,melt,2}$ was obtained using Eq. (3.2). The onset and end times of melting were consistent across all samples. Thus, t_0 and t_{end} were identical for all

measurements and therefore selected manually. The methods discussed in this subsection can be seen applied in the attached MATLAB file; Grid_enthalpy.m.

3.3 Fitting parameters for the Dual Nakamura model

The parameters were fitted by minimizing the normalized sum of squared errors, r^2. The Dual Nakamura model was evaluated against isothermal and non-isothermal measurements to secure a stable fit.

For the isothermal data, $t_{1/2}$, was extracted at the selected temperatures. Eq. (2.3) was used to fit U, K_g and R_0. The constants in Eq. (2.3) are listed in Table 3.7. Here, r^2_{iso} is the normalized squared error between the reciprocal of the measured $t_{1/2}$ values and the values predicted with Eq. (2.3).

For the non-isothermal data, cooling rates $\dot{T} = [20, 10, 5, 2, 1]$ K/min were used during fitting as training data and to determine the secondary Avrami exponent n_s afterwards, while $\dot{T} = [50, 40, 30, 0.5, 0.2]$ K/min were used for validation. Here, $r^2_{\text{non-iso}}$ is the normalized squared error between the measured non-isothermal relative crystallinity and the Dual Nakamura model Eq. (2.8). The combined error function is:

$$r^2 = w_{\text{iso}} r^2_{\text{iso}} + w_{\text{non-iso}} r^2_{\text{non-iso}} \tag{3.11}$$

The weights w_{iso} and $w_{\text{non-iso}}$ control the influence of each dataset to balance the fit. In this report, three different configurations for w_{iso} and $w_{\text{non-iso}}$ are tested: one solely dependent on isothermal data ($w_{\text{iso}} = 1$, $w_{\text{non-iso}} = 0$), one solely dependent on non-isothermal training data ($w_{\text{iso}} = 0$, $w_{\text{non-iso}} = 1$), and one with a balanced weighting between the datasets ($w_{\text{iso}} = 10$, $w_{\text{non-iso}} = 1$).

Initial guesses and bounds were set for each fitted parameter to ensure realistic solutions. An overview with sources is provided in Table 3.5.

Fitted parameter [unit]	Initial guess	Lower bound	Upper bound	Source
Pre-exponential factor, R_0 [1/s]	$4.82 \cdot 10^7$	10^4	10^8	[26]
Activation energy of crystallization, U [J/mol]	5439.2	4184	6694.4	[26]
Nucleation constant, K_g [K^2]	$2.11 \cdot 10^5$	10^4	10^7	[26]
Secondary Avrami exponent, n_s [−]	1.3	1	3	[5]

Table 3.5: Fitted parameters for Dual Nakamura model with initial guess and lower and upper bounds.

The method discussed in this subsection can be seen applied in the attached MATLAB file; "Dual_Nakamura_fit.m".

3.4 Numerical Approach

This section presents the numerical implementation required to translate the theory described in Chapter 2 into a functional finite element (FE) modelling framework. In this report, COMSOL Multiphysics is used as the FE software.

3.4.1 State Variables

This section describes the numerical methods used to model phase transitions with thermal hysteresis accurately. As discussed in Section 2.3.4, accounting for the thermal hysteresis of the material requires tracking the history of the temperature field over time. In COMSOL, this is efficiently handled using the State Variable feature. [9]

To maintain a record of the maximum temperature, a variable, T_{Max}, is defined. A state variable is initialized with the value $T_{\text{Max},0} = T_0$, corresponding to the initial temperature of the domain. This variable is subsequently updated at each time step and at every point in the domain according to the following criterion:

$$T_{\text{Max}} = \begin{cases} T & \text{if } T > T_{\text{Max}}, \\ T_{\text{Max}} & \text{otherwise.} \end{cases} \tag{3.12}$$

Eq. (3.12) determines the maximum temperature by comparing the temperature at the current time step with the value stored in the state variable. If the current temperature exceeds the stored value, the state variable is updated accordingly. Otherwise, it retains its value. This approach ensures that the maximum temperature is recorded for each point in the domain throughout the simulation.

Using the state variable T_{Max}, another state variable, HorC, is introduced to determine whether the material is being heated or cooled. This variable accounts for thermal hysteresis, ensuring that the latent heat of melting is not released once the material begins to cool, in Eq. (2.31).

The state variable HorC is initially set to 1, indicating that the material is being heated. It is updated according to the following logic:

$$\text{HorC} = \begin{cases} 1, & \text{if } T > T_{\text{Max}} - \text{tol}, \\ 0, & \text{if } T < T_{\text{Max}} - \text{tol and } T > T_{\text{ms}}, \\ \text{HorC}, & \text{otherwise.} \end{cases} \tag{3.13}$$

In Eq. (3.13) if the temperature falls below the maximum temperature minus a small tolerance ($\text{tol} = 10^{-3}$) to account for numerical noise, the state variable switches to 0, but only if the temperature is above the start temperature for melting, T_{ms}. This ensures that only the region actively undergoing a phase transition changes state and improves numerical stability.

3.4.2 Domain Representation

Following the approach in [43], the computational domain is simplified using the identity mapping function in COMSOL Multiphysics. Two geometries are defined in the simulation: the print bed, which serves as the computational domain where the theoretical framework in Chapter 2 is applied, and the printed part, which serves as the geometric domain.

An identity mapping function, defined in COMSOL [8] is used to project the location of the printed part from the geometric domain onto the computational domain. Within the computational domain, regions corresponding to the printed part are assigned a value of 1, while the remaining areas of the print bed are assigned 0. This mapping is then multiplied with the laser heat source in Eq. (2.14), ensuring that the laser only delivers heat to the regions where the part is located.

3.4.3 Mesh Generation and Optimization

With the identity mapping function, the computational domain is simplified to a rectangular box representing the print bed. Hexahedral elements were chosen for the mesh as they are well suited for rectangular geometries. A symmetric part is simulated, thus symmetry along the z-axis is used to shorten the computation time.

In regions influenced by the Gaussian laser heat source, the mesh element size is set to $H_{\max} = \sigma/2$, where σ is the standard deviation of the laser power distribution in Eq. (2.15). In regions outside the printed part, the mesh size is increased in steps to improve numerical efficiency as illustrated in Figure 3.8.

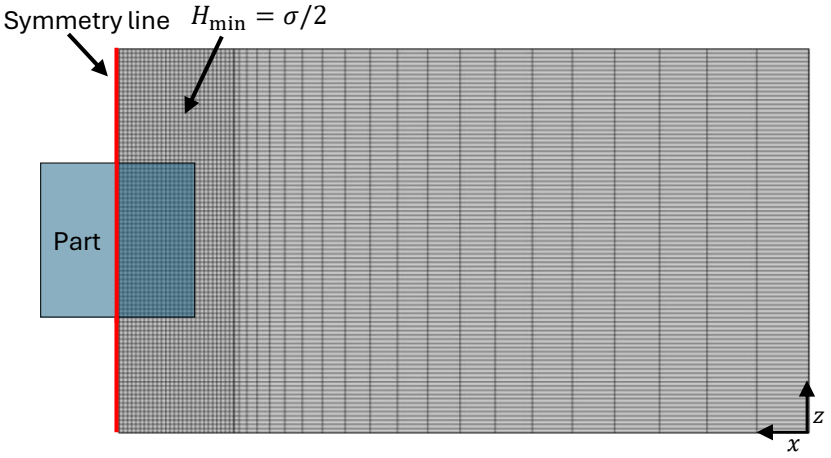

Figure 3.8: Illustration of the meshed computational domain.

3.4.4 Solver Configurations and Convergence

To ensure numerical stability, the CFL criterion must be satisfied, since the heat source moves upwards with the build velocity v_z. Based on the CFL condition [15], the maximum timestep during heating is restricted to:

$$\Delta t = \frac{1}{4} \cdot \frac{H_{\max}}{v_z}. \tag{3.14}$$

As discussed in Section 2.2.1, the Hoffman–Lauritzen equation (Eq. (2.3)) is only valid within the temperature range $T_\infty < T < T_m^\circ$. Outside this range, crystallization does not occur: either the temperature is too high for crystal formation, or it is low enough that the molecular chains are essentially immobile. Using Eq. (2.3) outside this range can lead to excessively high values and cause the solver to fail to converge. To prevent this, the equation is modified in COMSOL using the max operator:

$$\max\left(T_m^\circ - T,\, 10^{-6}\right) \quad \wedge \quad \max\left(T - T_\infty,\, 10^{-6}\right) \tag{3.15}$$

This operator ensures that the larger value between $T_m^\circ - T$ and 10^{-6} is used in Eq. (2.3), effectively setting the reaction rate to a numerical zero when the temperature is outside the valid range. Finally, the time-dependent solver is configured with a relative tolerance of 10^{-4}, ensuring sufficiently small time-steps to maintain numerical stability and convergence, while preserving computational efficiency.

3.4.5 Parameters

The parameters used for the Dual Nakamura model and the thermal print scale model are summarized in Table 3.6 and Table 3.7.

Property	Value	Unit (Symbol)	Source
Absorption coefficient, K	0.8	[−]	[−]
Attenuation length, γ	$1.11 \cdot 10^4$	[m]	[35][1]
Avg. Laser Power, P_0	20	[W]	[−]
Avg. Laser Scanning Speed, v_{laser}	1.1	[m/s]	[16]
Base specific heat capacity, $c_{p,0}$	2.3	[kJ/(kg · K)]	[Section 4.1.1]
Bulk density, ρ_{bulk}	540	[kg/m^3]	[49]
Convection coefficient build platform, h_{side}	10	[W/(m^2·K)]	[27]
Convection coefficient of sides, h_{side}	10	[W/(m^2·K)]	[27]
Convection coefficient top, h_{air}	15	[W/(m^2·K)]	[35]
Density of solid material, ρ_{solid}	1100	[kg/m^3]	[49]
Duration of cooling, Δt_{cool}	145	[min]	[−]
Emissivity, ϵ	0.95	[−]	[7]
Hatch spacing, h_{hatch}	0.36	[mm]	Sinterit Studio
Initial temperature, T_0	187	[°C]	Sinterit Studio
Layer grouping factor, n_{layer}	10	[−]	[−]
Layer height, h_{layer}	0.125	[mm]	Sinterit Studio
Latent heat of crystallization, $\Delta H_{\infty,cry}$	40.57	[J/g]	[Section 4.1.4]
Latent heat of melting, $\Delta H_{\infty,\text{melt}}$	55.23	[J/g]	[Section 4.1.1]
Phase transition parameter, b	0.5	[−]	[42][1]
Temperature of air, T_{air}	T_0	[°C]	[−]
Temperature of build platform, T_{side}	175	[°C]	Sinterit Studio
Temperature of melting start, T_{ms}	196	[°C]	[Section 4.1.1]
Melting temperature, T_m	203.2	[°C]	[Section 4.1.1]
Standard deviation of the Gaussian distribution, σ	$n_{\text{layer}} \cdot \gamma$	[mm]	[−]
Thermal conductivity of solid, k_{solid}	0.28	[W/(m · K]	[31][2]
Vertical print velocity, v_z	14	[mm/h]	[41]

Table 3.6: Summary of thermal parameters used in the print-scale simulation.

Property	Value	Unit (Symbol)	Source
Activation energy of crystallization, U	4184	[J/mol]	Table 4.2
Equilibrium melting temperature, T_m°	493	[K]	[25][2]
Glass Transition Temperature, T_g	316	[K]	[25][2]
Nucleation constant, K_g	3.842×10^5	[K^2]	Table 4.2
Pre-exponential factor, R_0	4.82×10^7	[1/s]	Table 4.2
Primary Avrami exponent, n_p	3.12	[−]	Section 4.1.2
Secondary Avrami exponent, n_s	1.15	[−]	Table 4.2

Table 3.7: Summary of Crystallization Parameters for the Dual Nakamura Model

1 Value from PA12, as no data were available for PA11-CF.
2 Value from PA11, as no data were available for PA11-CF.

4 RESULTS AND DISUSSION

This chapter presents, analyzes, and discusses the key findings of the experiments, parameter fitting, and numerical modeling. The resulting print-scale, thermal–crystallization simulation is assessed based on the temperature evolution and crystallization kinetics.

4.1 Experimental results

This section summarizes the experimental findings obtained from the DSC analyses of PA11-CF powder and sintered material. The presented results provide the thermal- and crystallization-parameters required to implement the material into a numerical model, and derive proper fitting parameters for the Dual Nakamura model.

4.1.1 Specific Heat Measurements

Figure 4.1 presents the heat flow results from the three DSC experiments in Section 3.2.1, along with the mean curve and the blank reference. The measurements are consistent across all three experiments, showing an endothermic peak at $T_m = 203.2$ °C during melting. A negative exothermic peak occurs at $T_c = 166$ °C during crystallization. These results reveal the material's thermal hysteresis and indicate a wide working temperature range at the specified heating and cooling rate.

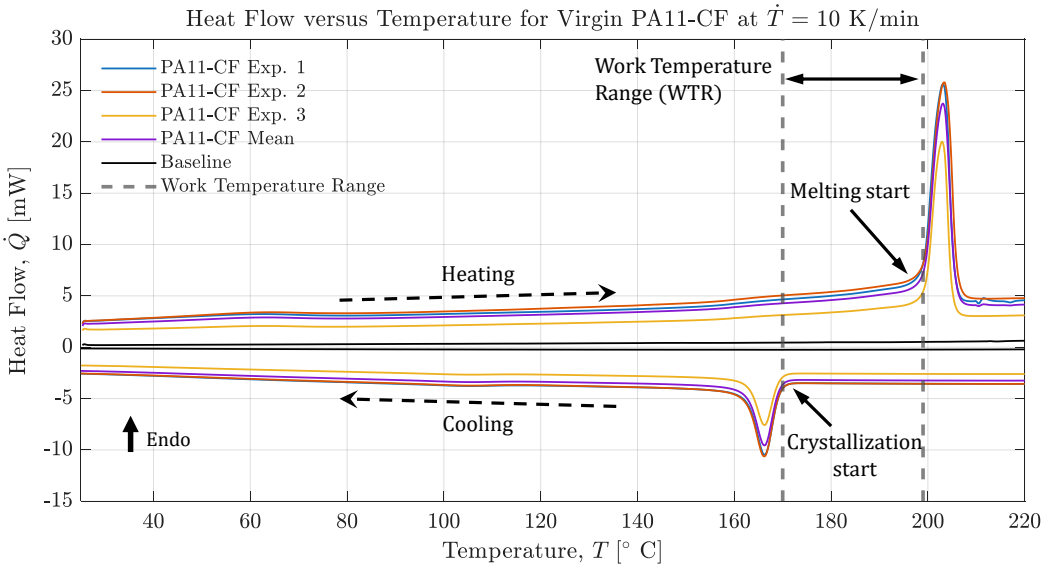

Figure 4.1: Heat flow versus temperature for virgin PA11-CF obtained through DSC with $\dot{T} = 10$ K/min and corrected baseline.

From the data in Figure 4.1, the averaged effective specific heat, $\bar{c}_p$, was calculated using Eq. (3.7). The resulting heating and cooling curves, shown in Figure 4.2, display the expected thermal behavior: a relatively constant specific heat outside the phase change region and sharp peaks corresponding to melting and crystallization. The curves also allow determination of key transition temperatures, including the melting onset at $T_{ms} = 196$ °C and the peak melting temperature at $T_m = 203.2$ °C. Furthermore, the peak in effective specific heat during melting is notably larger than the peak during crystallization. This suggests that the material undergoes a heat treatment that increases its crystallinity, as an equally high crystallinity is not achieved by cooling the powder at a rate of $\dot{T} = 10$ °C.

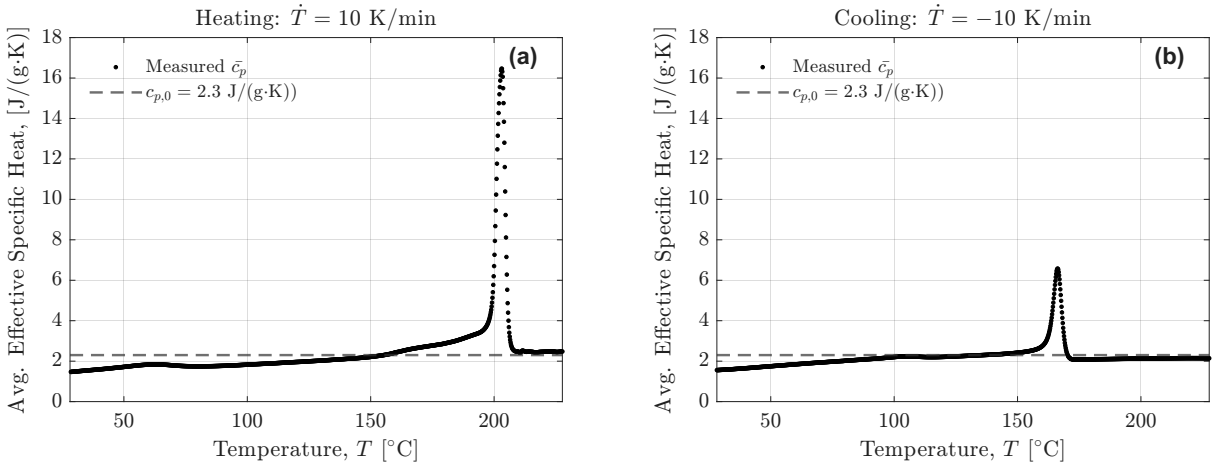

Figure 4.2: Averaged specific heat capacity, $\bar{c_p}(T)$, of virgin PA11-CF determined with baseline correction during heating, (a), and cooling (b).

In Section 2.3.4, a constant base specific heat of $c_{p,0} = 2.3$ was assumed, indicated by the dashed line in Figure 4.2b. The results show that the base specific heat increases with temperature in the solid state but remains nearly constant after melting. The chosen value of $c_{p,0} = 2.3$ captures the thermal response sufficiently, as the base specific heat does not vary significantly with temperature. A more detailed model incorporating this temperature dependence could be developed in future work, but it falls beyond the scope of this project.

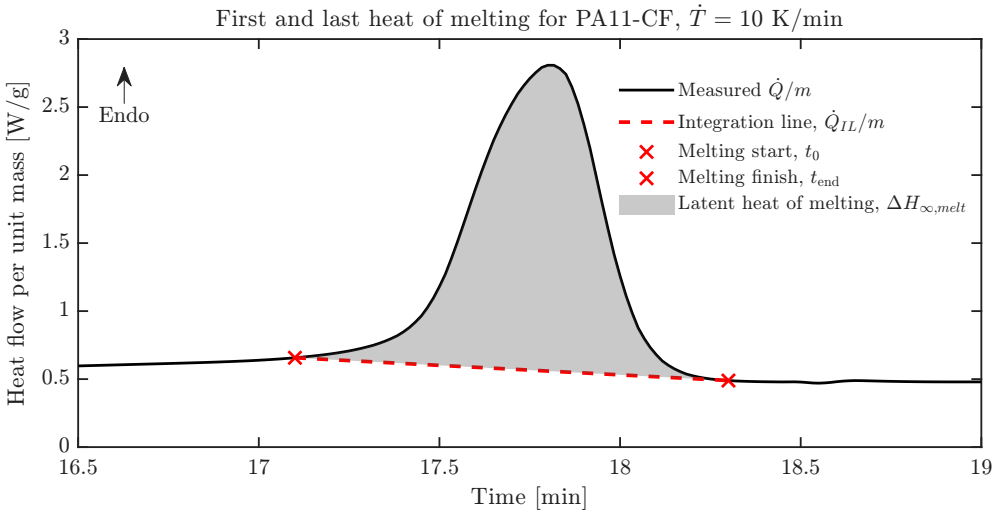

Figure 4.3: Full melting curve with integration line used for determining the first latent heat of melting.

The latent heat of melting $\Delta H_{\infty,melt}$ is found from the data in Figure 4.1 using the method described in Section 3.2, with the integration area shown in Figure 4.3. The resulting latent heat of melting is calculated to $\Delta H_{\infty,melt} = 55.23\ \mathrm{J/g}$.

4.1.2 Isothermal crystallization

The results of the isothermal DSC analysis described in Section 3.2.2 are shown in Figure 4.4. Here, $\dot{Q}_{rel}$ represents the relative heat flow. Outside the crystallization range, $\dot{Q}(t)$ is expected to be zero during annealing. Due to measurement noise, the recorded data showed $\dot{Q}(t) \neq 0$ in these regions. To correct this, a constant offset was applied: $\dot{Q}_{rel} = \dot{Q} - c$, where c corresponds to the heat flow when the slope reached zero after the crystallization peak, indicating that crystallization was complete. $\dot{Q}_{rel}$ is used solely for visualization purposes.

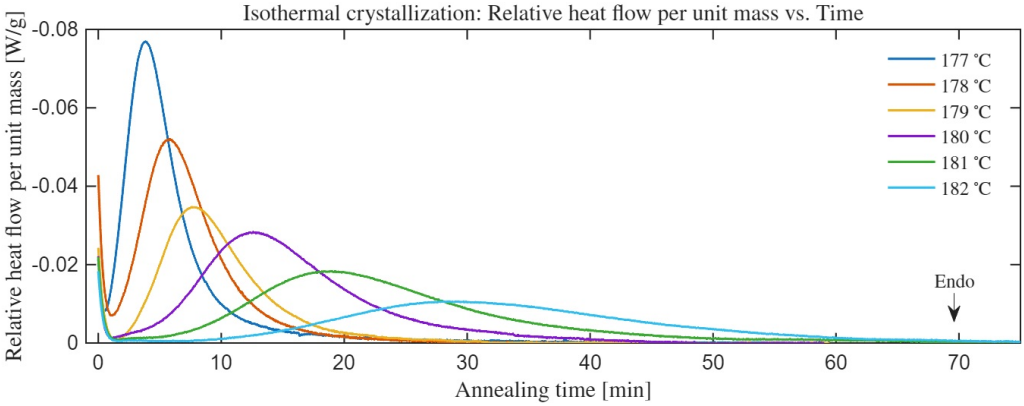

Figure 4.4: $(t, \dot{Q})$ results from isothermal DSC analysis

Figure 4.4 shows that the crystallization process is longer for higher annealing temperatures. This is evident from the heat flow curves; e.g., data for $T_{target} = 182\ ^\circ\mathrm{C}$ shows a broader and flatter curve compared to the sharper curve for $T_{target} = 177\ ^\circ\mathrm{C}$. The experiments at $T_{target} = 177^\circ C$ and $T_{target} = 178^\circ C$ do not reach a relative heat flow of zero before annealing, indicating that crystallization had already started before T_{target} was reached. This is because the maximum cooling rate of 60 $\frac{\mathrm{K}}{\mathrm{min}}$ for the DSC machine, was too low. Consequently, results for $T_{target} = 177^\circ C$ and $T_{target} = 178^\circ C$ are excluded from further analysis. For future work, isothermal experiments should be performed using flash DSC, which achieves higher cooling rates and allows lower annealing temperatures. Using flash DSC was, however, beyond the scope of this project.

$T_{\mathrm{target}}[^\circ\mathrm{C}]$	$t_{\mathrm{hold}}[\mathrm{min}]$	$t_{\frac{1}{2}}[\mathrm{min}]$
179	60	7.437
180	120	13.55
181	120	19.92
182	180	25.29

Table 4.1: $t_{1/2}$ results for the 4 highest annealing temperatures

The results for $t_{1/2}$ are listed in Table 4.1 and confirm that the crystallization process slows down at higher annealing temperatures. An example of how $t_{1/2}$ is determined for $T_{target} = 179$ °C is shown in Figure 4.5.

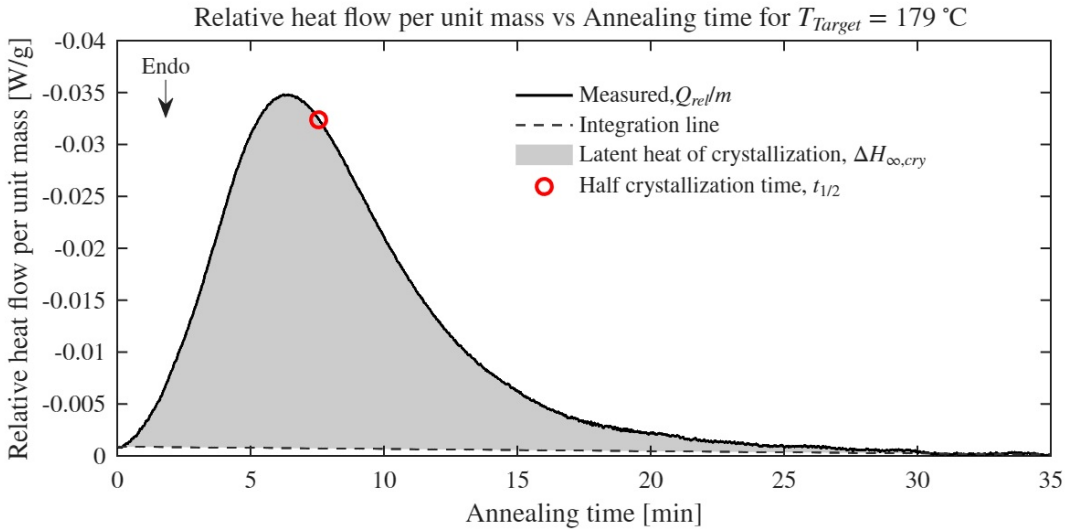

Figure 4.5: Example of determining $t_{1/2}$ from a $(t, \dot{Q})$ plot.

From Figure 4.5, it is apparent that the measurements exhibit some noise at the end of the crystallization. This is due to the minimal heat flow during the final stage of crystallization, where noise has a greater impact. Additionally, the curves are asymmetric, and $t_{1/2}$ is located to the right of the peak, indicating that latent heat is released over a longer period at the end than at the beginning.

Following the method of Section 3.2.2. The Avrami exponent has been fitted for primary crystallization $\alpha_{cry}(t) \in [0.05, 0.25]$ The fit can be seen in Figure 4.6.

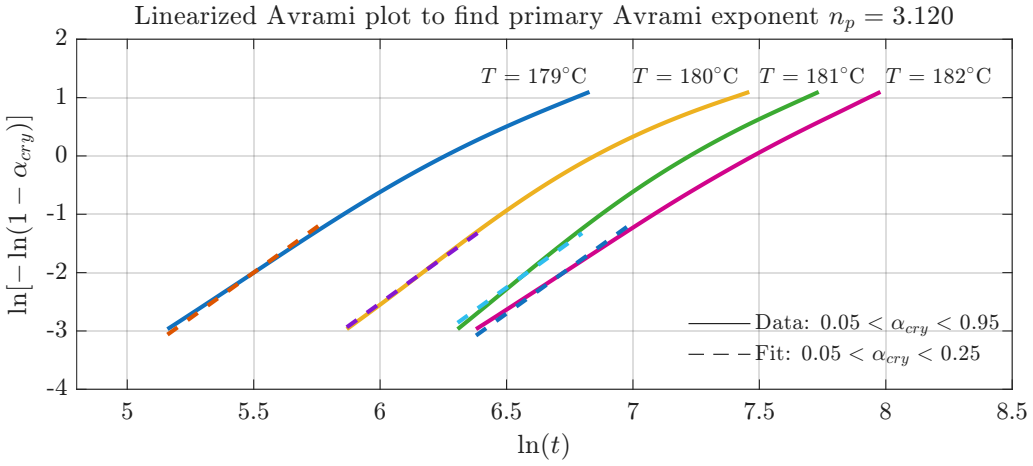

Figure 4.6: Linearized Avrami plot to find primary Avrami exponent. $n_p = 3.120$

The results show that splitting the crystallization model into a primary and a secondary contribution is advantageous. For $\alpha_{cry}(t) > 0.25$ the data stops following a linear trend. As $\alpha_{cry}(t)$ increases beyond 0.25 the slope decreases, which indicates growing influence from slower secondary crystallization. Within the fitted range $\alpha_{cry}(t) \in [0.05, 0.25]$ the data is linear

and follows the fit for all isothermal temperatures. The optimal primary Avrami exponent for all temperatures was $n_p = 3.120$, and this value is used in the Dual Nakamura model.

4.1.3 Non-isothermal crystallization

The results from the non-isothermal DSC experiments in Section 3.2.3 are shown in Figure 4.7. The data reveal a clear correlation between cooling rate and crystallization: increasing the cooling rate shifts the crystallization curves to lower temperatures.

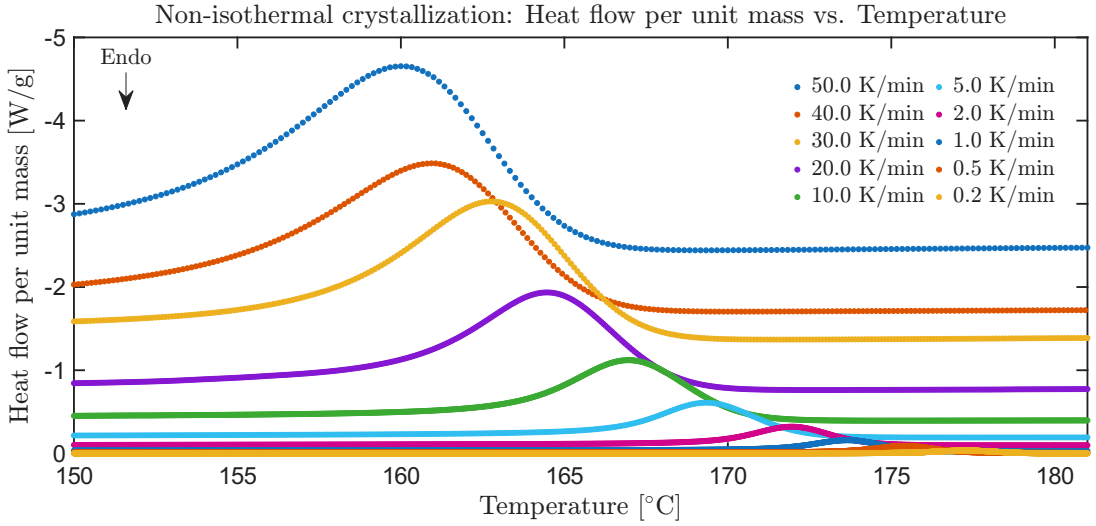

Figure 4.7: Results from non-isothermal DSC analysis ranging from $\dot{T}$ = 50 to 0.2 $\frac{\text{K}}{\text{min}}$

The method described in Section 3.2.3 was used to determine the relative crystallinity, $\alpha_{\text{cry}}(t)$. Figure 4.8 presents α_{cry} for all measured cooling rates. The crystallization curve exhibits a sigmoidal-shape, with a sharper slope at the beginning than at the end, indicating that rapid primary crystallization dominates initially, while secondary, slower crystallization, governs the later stage.

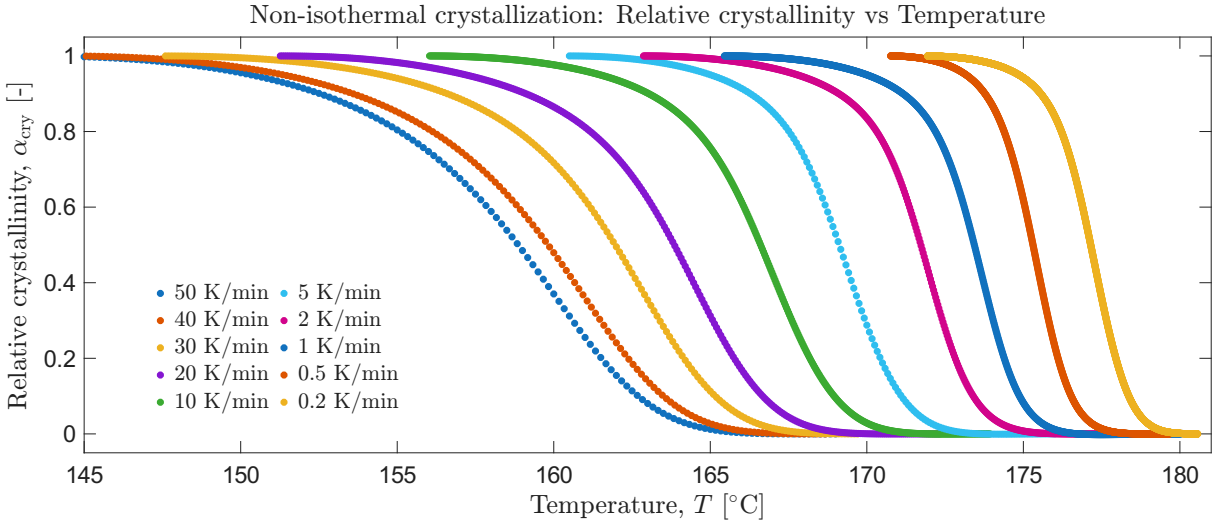

Figure 4.8: Relative crystallinity from DSC analysis for cooling rates ranging from $\dot{T}$ = 50 to 0.2 $\frac{\text{K}}{\text{min}}$

4.1.4 Part location effect on degree of crystallinity

The results from the DSC experiments in Section 3.2.4 show the second latent heat of melting, $\Delta H_{\infty,\text{melt},2}$, which is equivalent to the latent heat of crystallization obtained during printing, plotted against the absolute distance from the central cube M3 in Figure 4.9.

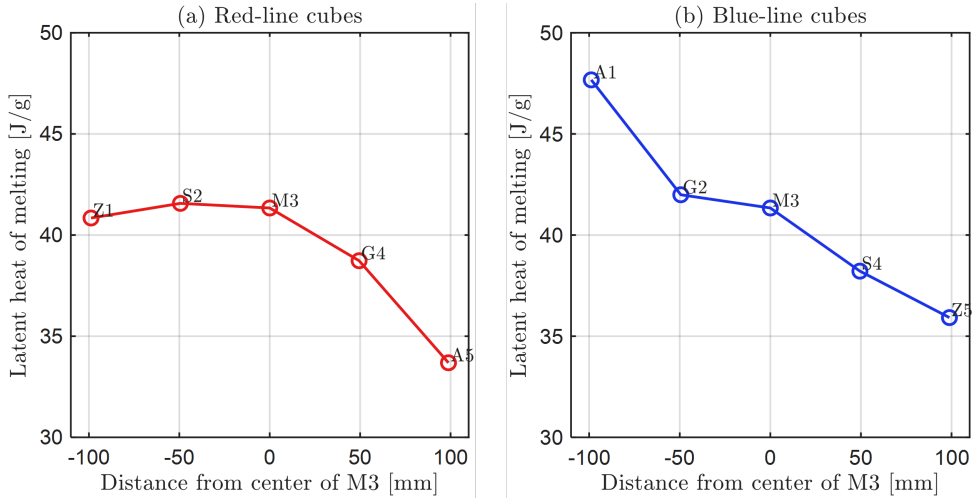

Figure 4.9: Second latent heat of melting $\Delta H_{\infty,melt,2}$ as a function of distance from the central M3 reference point. Subplot (a) shows the red-line cubes, while (b) shows the blue-line cubes. Each data point is labeled with the cube identifier, and the spatial distance reflects the physical layout of the sample during the heating experiment.

Figure 4.9 shows a slight positional dependence in latent heat. Along the red diagonal, the cubes printed at the top of the print bed exhibit the lowest latent heat, suggesting reduced crystallinity, while cubes closer to the middle show higher latent heat. A similar trend is observed along the blue diagonal, where the upper-layer cubes again show lower latent heat than those located deeper in the print bed. Cube $A1$, however, appears to be an outlier, exhibiting a much higher latent heat than all other cubes. The mid- and bottom-layer cubes generally display the highest latent heat values, consistent with slower cooling and therefore more complete crystallization in those regions. Because only a small subset of the 125 cubes was analyzed, these results cannot fully resolve the influence of print position on crystallinity. Additional experiments would be required to do so, which is beyond the scope of this project.

The assumption of a constant latent heat of crystallization is sufficient for the purposes of this study, as described in Section 2.3.4. From the results in Figure 4.9, the average second latent heat of melting, $\Delta H_{\infty,\text{melt},2} = \Delta H_{\infty,\text{cry}} = 40.57\ \frac{\text{J}}{\text{g}}$, is obtained.

It should also be noted that two of the heat flow measurements, shown in Figure 4.10, yielded poor results, presumably due to insufficient thermal contact between the sample and crucible. These errors highlight underlying experimental uncertainties that must be controlled before more definitive conclusions can be drawn. Performing additional experiments would help reduce these uncertainties.

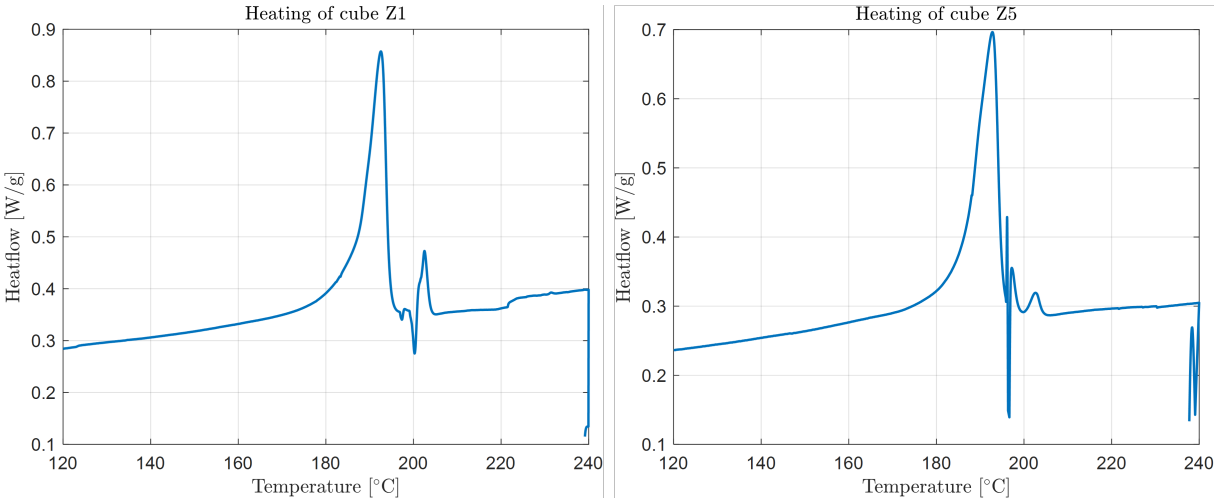

Figure 4.10: Flawed heat flow curves for cube Z1 and Z5, obtained from DSC

4.1.5 Results for Fitting the Dual Nakamura Model

Having obtained data of $\alpha_{cry}(t)$ for both non-isothermal and isothermal crystallization, $t_{1/2}$ and n_p, the fitting of R_0, U, K_g and n_s can be carried out as decribed in Section 3.3.

The resulting fitted parameters for the configurations,describedSection 3.3, can be found in Table 4.2.

Configuration	$R_0[\frac{1}{s}]$	$U[\frac{J}{mol}]$	$K_g[K^2]$	n_s
1: $w_{iso} = 1 \wedge w_{non-iso} = 0$	$4.82 \cdot 10^7$	6694.4	$3.367 \cdot 10^5$	2.097
2: $w_{iso} = 0 \wedge w_{non-iso} = 1$	$4.82 \cdot 10^7$	4184	$3.842 \cdot 10^5$	1.15
3: $w_{iso} = 10 \wedge w_{non-iso} = 1$	$4.82 \cdot 10^7$	4794.83	$3.744 \cdot 10^5$	1.152

Table 4.2: Results for fitted parameters for Dual Nakamura model.

In Figure 4.11 to Figure 4.13, configurations 1 to 3 are shown, respectively. To evaluate the fit, the $R_C = 1/t_{1/2}$ data as well as the non-isothermal training and validation data, described in Section 3.3, are plotted against the model fits.

Configuration 2 (Figure 4.12) and 3 (Figure 4.13) generally agree with the non-isothermal validation and training data. Configuration 1 (Figure 4.11) performs poorly for both the non-isothermal validation and training data; however, the R_C fit shows a stronger correlation between model and $t_{1/2}$-data than the other configurations. The poor performance of the Dual Nakamura model for configuration 1 could suggest that the setup used to acquire the isothermal crystallization data was suboptimal. Utilizing a Flash DSC machine could potentially improve the quality of the isothermal measurements but is beyond the scope of the project.

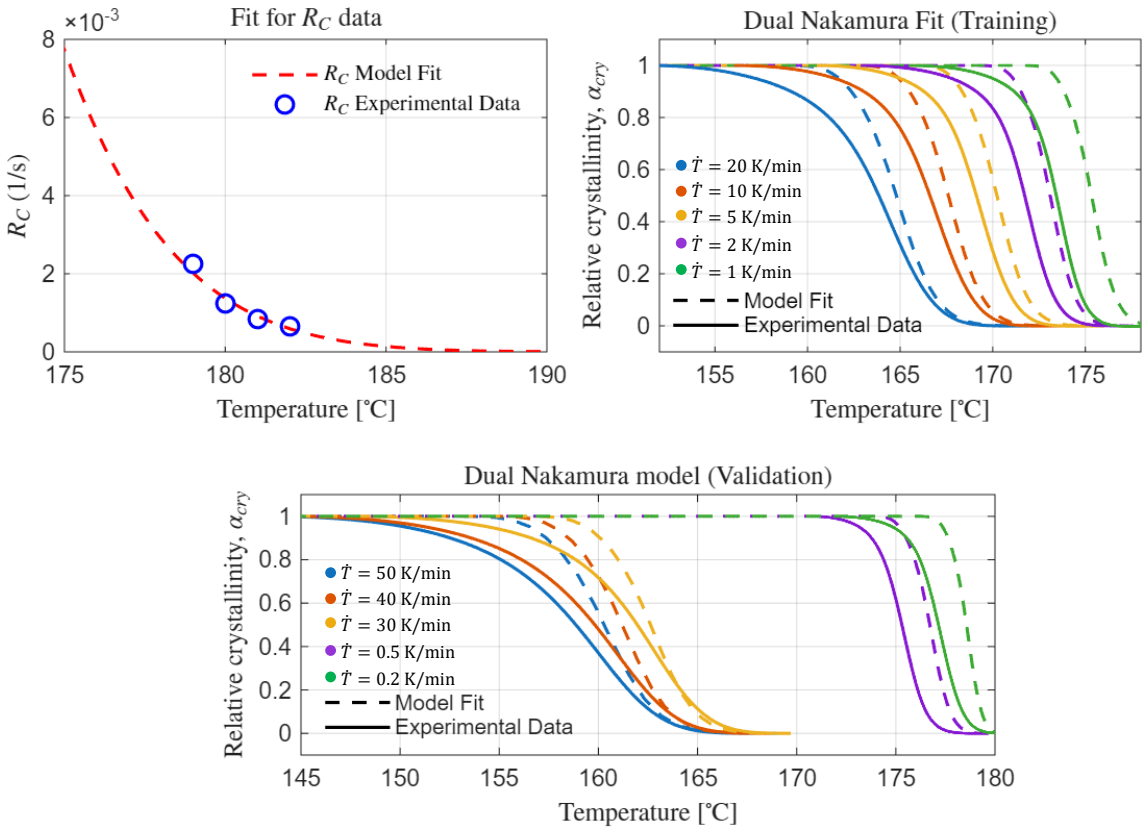

Figure 4.11: Model fits for Dual Nakamura model with $w_{iso} = 1$ and $w_{non-iso} = 0$

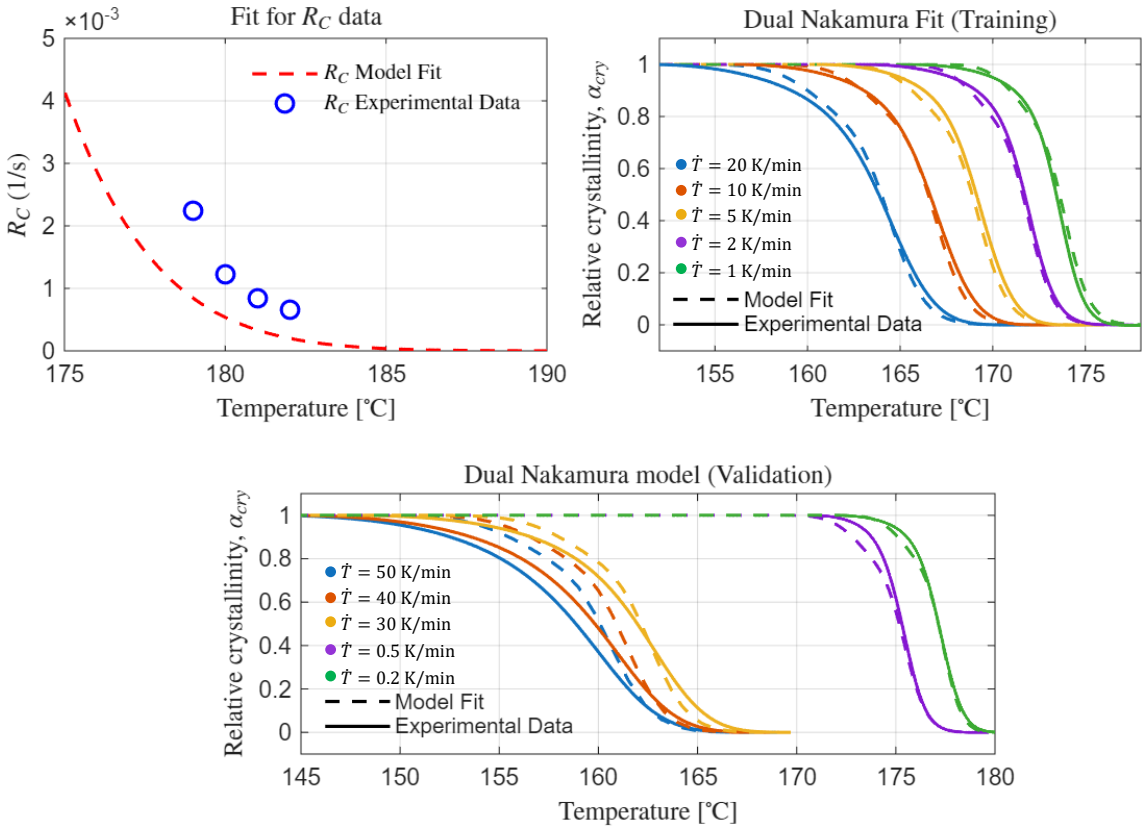

Figure 4.12: Model fits for Dual Nakamura model with $w_{iso} = 0$ and $w_{non-iso} = 1$

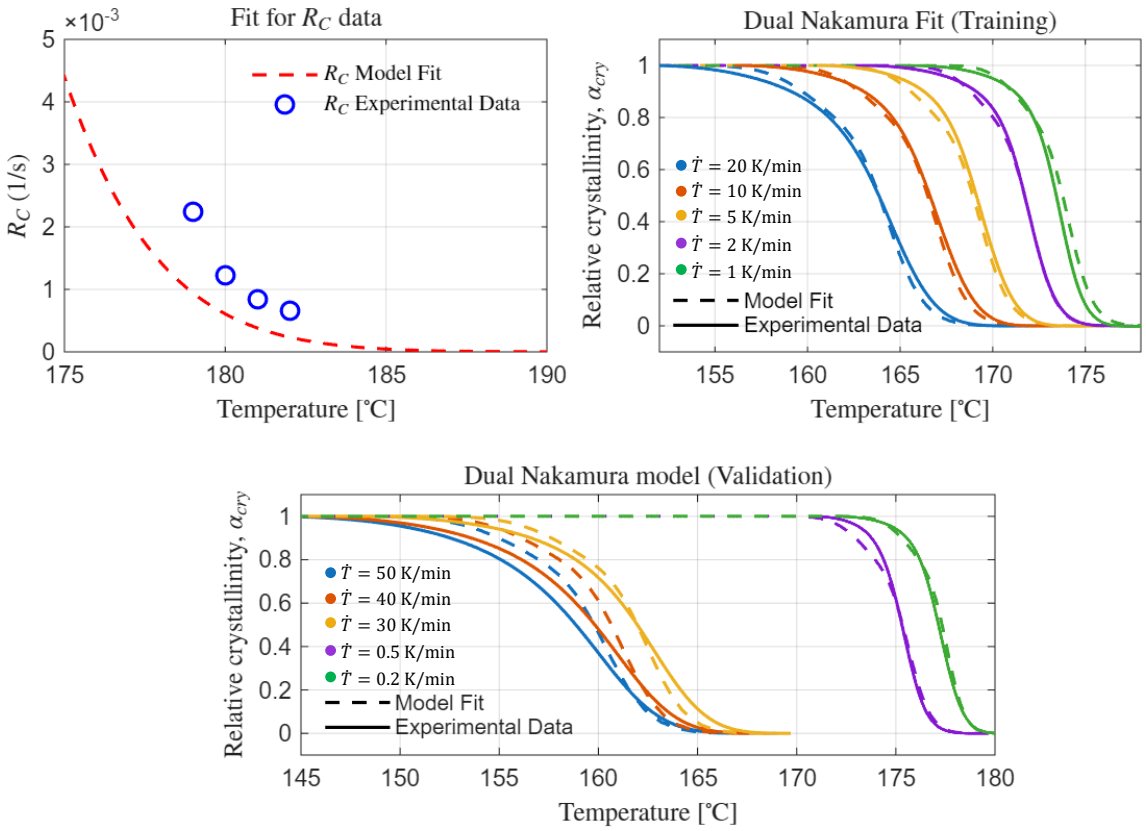

Figure 4.13: Model fits for Dual Nakamura model with $w_{iso} = 10$ and $w_{non-iso} = 1$

Results from configurations 2 and 3 are very similar. Both configurations exhibit poor modeling at the highest cooling rates, $\dot{T} = [50, 40, 30]$ K/min. Because this report focuses on supporting thermal modeling for SLS printing, where such high cooling rates are unlikely, accurate modeling at lower cooling rates is more relevant. Cooling in an SLS printer is expected to be closer to $\dot{T} = [0.5, 0.2]$ K/min. Configuration 2 models the lower cooling rates more accurately than configuration 3, particularly for primary crystallization at higher temperatures. Configuration 2 therefore provides the best overall agreement between data and model across all plots. For this reason, the parameters obtained from configuration 2 will be used in the print-scale SLS model.

4.2 Numerical results

This section evaluates the results obtained from implementing the Dual Nakamura model into the thermal SLS print-scale model. A 2D simulation was performed in COMSOL Multiphysics, analyzing a simple square with side lengths, 20 mm. The computation time was 2 min and 25 s on a Lenovo ThinkPad with 32 GB of RAM and 16 cores.

Figure 4.14 shows the maximum temperature reached at each point during the printing process. The highest temperatures occur at the center of the printed part, while a mild gradient is observed across the edges of the printed part. The temperature gradient at the bottom is broader than at the top and sides, resulting in an asymmetric profile around the x-axis.

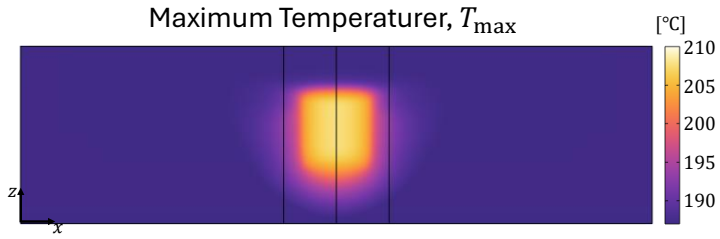

Figure 4.14: Maximum temperature reached at each point during the printing process

This behavior can be attributed to the heat sink effect of the unsintered powder. At the bottom, the laser initially heats a large volume of powder, which absorbs and distributes heat, reducing the local temperature rise. As the print progresses, residual heat from previous sintered layers reduces this heat sink effect, resulting in a broader thermal gradient at the bottom than at the top.

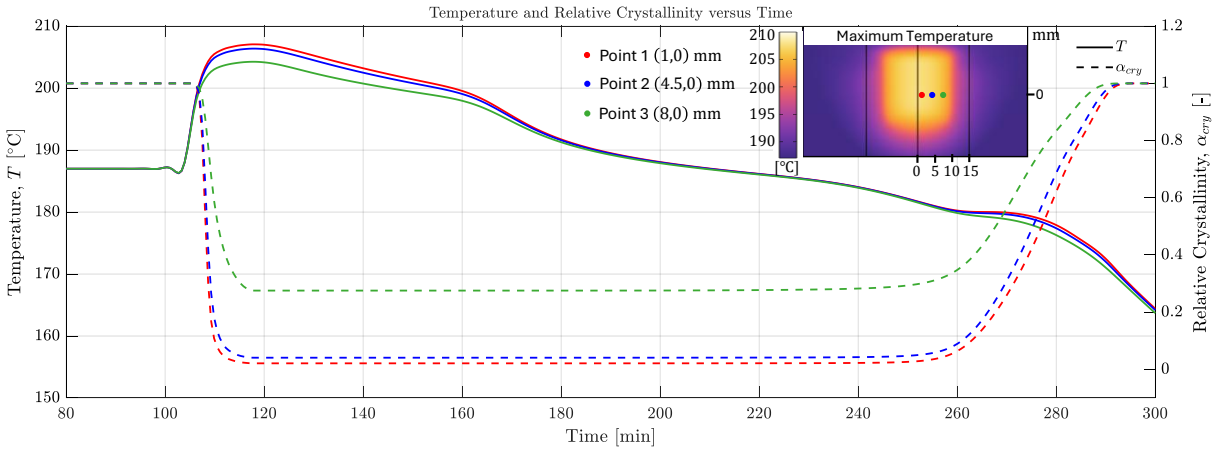

Figure 4.15: Point temperature and relative crystallinity as functions of time during the printing process

In Figure 4.15, the temperature and relative crystallinity are shown as functions of time for three points inside the printed part, located at different distances from the right edge of the part. The point close to the edge reaches a lower peak temperature. This is caused by the large temperature gradient between the sintered and unsintered powder at the edge, which acts as a heat sink and lowers the peak temperature. The continuous print-scale approach amplifies this effect. In the print-scale model, heat is applied over a longer period than in actual SLS. This slower heating allows the powder to distribute heat more effectively, whereas in the actual SLS process, rapid heating limits the time available for thermal conduction. As a result of this, the numerical model will underestimate the peak temperatures.

During crystallization, the point closest to the edge of the printed part cools faster. The exothermal heat relased during the phase transtion escapes more readily into the surrounding unsintered powder at this location. Additionally, since the melting phase transformation is not fully complete at the edge, due to lower peak temperatures, less latent heat is released during crystallization. Consequently, from $t = 240$ min to $t = 270$ min, when most crystallization occurs, the temperature at the edge is noticeably lower than at points closer to the center.

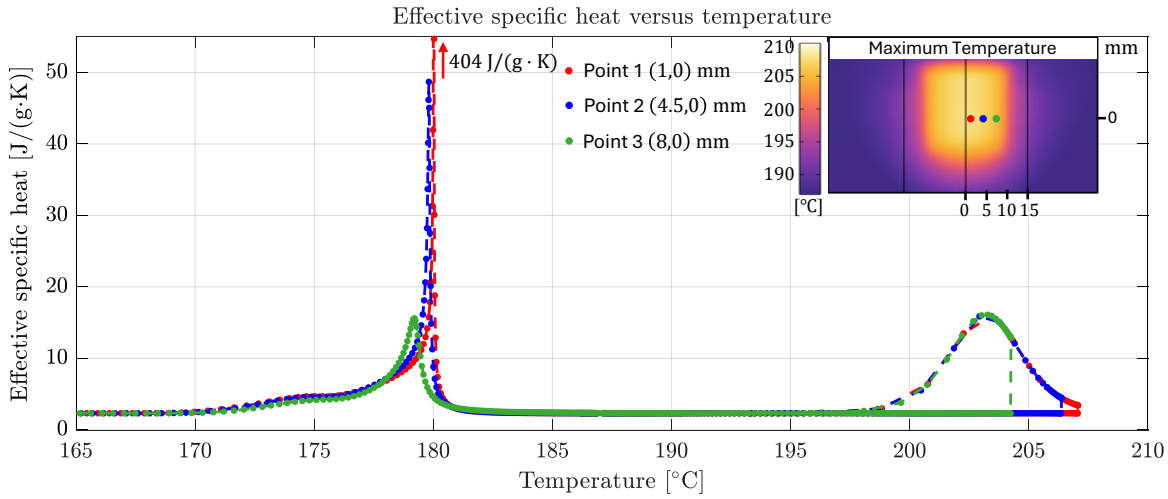

Figure 4.16: Effective specific heat versus temperature measured at three points during the printing process

In Figure 4.16, this trend is also evident. Points near the center undergo a more complete phase transition than points near the edge. During crystallization, the center exhibits a pronounced peak in effective specific heat, indicating heat accumulation in this region. This leads to near-isothermal conditions at the beginning of crystallization in the center, while crystallization at the edge occurs under more non-isothermal conditions.

The results show that the Dual Nakamura model works within the print-scale thermal framework to link temperature history to crystallinity with stable behavior. The extended energy input allows for a more efficient simulation but smooths the rapid heating seen in the actual SLS process. This lowers peak temperatures and limits melt completion near the edges. Future work should explore methods to capture higher peak temperatures while maintaining computational efficiency. The framework however provides a strong basis for guiding process parameter selection and part placement, forming a foundation for improving consistency and mechanical performance of SLS printed parts.

5 CONCLUSION

This project developed a coupled thermal and crystallization model for selective laser sintering of carbon fiber-reinforced PA11. Material-specific thermal properties and crystallization kinetics were obtained through extensive experimental DSC work.

Isothermal DSC measurements showed increasing crystallization half-time with higher annealing temperatures, indicating slower crystallization near the melting point. Analysis of the Avrami exponent indicated that it was not constant throughout crystallization. The material exhibited primary and secondary crystal growth. Primary growth dominated early stages with rapid growth $n_p = 3.12$, while secondary growth was slower with $n_s = 1.15$, dominating in the later stages of crystallization. These observations justified the use of a Dual Nakamura model to capture both primary and secondary crystallization behaviors.

Non-isothermal measurements revealed a strong dependence of crystallization kinetics on cooling rate, with crystallization occurred at lower temperatures with higher cooling rates. Measurements on sintered cubes from different build locations indicated variation in crystallization enthalpy. Although the dataset was limited, the results suggest a potential location-dependent effect on the degree of crystallization within the printer.

Model parameters for the dual-Nakamura model were fitted using different combinations of weighted isothermal and non-isothermal data. When fitted to only non-isothermal data, the model showed good agreement with validation data at low cooling rates ($\dot{T} = 0.5, 0.2\ \frac{\mathrm{K}}{\mathrm{min}}$). At high cooling rates ($\dot{T} = 50, 40, 30\ \frac{\mathrm{K}}{\mathrm{min}}$) none of the fits accurately captured crystallization. Since such high cooling rates are not expected in SLS printing process, the model fitted to only non-isothermal data was selected for further use.

Integration of the crystallization kinetics into a print-scale heat transfer model allowed simultaneous prediction of temperature evolution, phase change, and crystallinity development during the SLS process. The results show that experimentally calibrated crystallization kinetics can be successfully coupled with thermal simulations for PA11-CF. Points near the center of the parts experienced higher peak temperatures, and during crystallization, heat accumulation led to near-isothermal behavior initially. Heat escapes more easily at points near the edges, leading to more non-isothermal crystallization. The efficient simulation approach also smooths the rapid heating observed in actual SLS processes. Including a more accurate representation of melt kinetics could further improve simulation accuracy. In the end, the developed numerical-experimental framework provides a solid basis for predicting spatial variations in temperature and crystallinity during printing and cooling, which can guide more reliable processing and improve the mechanical performance of SLS-printed parts.

BIBLIOGRAPHY

[1] Loughborough University Additive Manufacturing Research Group. *About Additive Manufacturing: Powder Bed Fusion*. https://www.lboro.ac.uk/research/amrg/about/the7categoriesofadditivemanufacturing/powderbedfusion/. 2023.

[2] Omar Al-Qatami and Gianfranco Mazzanti. "The effect of the sample pan position on the determination of the specific heat capacity for lipid materials using heat flux DSC." In: *Thermochimica Acta* 710 (2022), p. 179148. ISSN: 0040-6031.

[3] Melvin Avrami. "Kinetics of Phase Change. I General Theory." In: *The Journal of Chemical Physics* 7.12 (Dec. 1939), pp. 1103–1112. ISSN: 0021-9606. DOI: 10.1063/1.1750380. eprint: https://pubs.aip.org/aip/jcp/article-pdf/7/12/1103/18791257/1103_1_online.pdf.

[4] Melvin Avrami. "Kinetics of Phase Change. II Transformation-Time Relations for Random Distribution of Nuclei." In: *The Journal of Chemical Physics* 8.2 (Feb. 1940), pp. 212–224. ISSN: 0021-9606. DOI: 10.1063/1.1750631. eprint: https://pubs.aip.org/aip/jcp/article-pdf/8/2/212/18791481/212_1_online.pdf.

[5] Melvin Avrami. "Granulation, Phase Change, and Microstructure Kinetics of Phase Change. III." In: *The Journal of Chemical Physics* 9.2 (Feb. 1941), pp. 177–184. ISSN: 0021-9606. DOI: 10.1063/1.1750872.

[6] "7 - Powder bed fusion of polymers." In: *Laser Additive Manufacturing*. Ed. by Milan Brandt. Woodhead Publishing Series in Electronic and Optical Materials. Woodhead Publishing, 2017, pp. 181–204. ISBN: 978-0-08-100433-3. DOI: https://doi.org/10.1016/B978-0-08-100433-3.00007-5.

[7] Christian L. Budden, Kenneth Æ. Meinert, Aakil R. Lalwani, and David B. Pedersen. "Chamber Heat Calibration by Emissivity Measurements in an Open Source SLS System." In: *2022 ASPE and euspen Summer Topical Meeting on Advancing Precision in Additive Manufacturing*. American Society for Precision Engineering, 2022, pp. 180–185.

[8] COMSOL AB. *Identity Mapping*. https://doc.comsol.com/5.5/doc/com.comsol.help.comsol/comsol_ref_definitions.12.076.html. COMSOL Multiphysics Reference Manual 5.5. COMSOL AB, 2019.

[9] COMSOL Multiphysics. *How to Use State Variables in COMSOL Multiphysics*. Accessed: 2024-12-28. n.d.

[10] W. D. Callister and D. G. Rethwisch. "Materials Science and Engineering: An Introduction." In: 9th. Hoboken, NJ: Wiley, 2014. Chap. 14–15.

[11] Dietmar Drummer, Dominik Rietzel, and Florian Kühnlein. "Development of a characterization approach for the sintering behavior of new thermoplastics for selective laser sintering." In: *Physics Procedia* 5 (2010). Laser Assisted Net Shape Engineering 6, Proceedings of the LANE 2010, Part 2, pp. 533–542. ISSN: 1875-3892. DOI: https://doi.org/10.1016/j.phpro.2010.08.081.

[12] Maotiao Gao, Shiqi Zhao, Hongjun Yang, Xuehong Wu, and Yingjie Xiao. "An Analysis of the Influence of DSC Parameters on the Measurement of the Thermal Properties of Phase-Change Material." In: *Materials* 17.23 (2024). ISSN: 1996-1944. DOI: 10.3390/ma17235689.

[13] Julien Gardan. *Additive manufacturing technologies: State of the art and trends*. Ed. by Adedeji B. Badiru, Vhance V. Valencia, and David Liu. Boca Raton, FL: CRC Press, 2017, pp. 149–168. ISBN: 978-1-315-11910-6. DOI: 10.1201/9781315119106-10.

[14] priomold GmbH. *Materials – Selective Laser Sintering (SLS)*. https://www.priomold.com/fileadmin/user_upload/Unterseite_3D-Druck/UEbersichten/priomold-materials-SLS.pdf. Accessed: 2025-11-11. 2024.

[15] Caminha Guilherme. *The CFL Condition and How to Choose Your Timestep Size*. Accessed: 2025-11-25. SimScale. 2024.

[16] J. Hesselvig, R.T. Nygaard, M.K. Budzik, and M. Sandberg. "Efficient continuum-based modelling and analysis of polymer SLS: Insights into particle sintering and densification in straight and corner scanning passes." In: *Additive Manufacturing* 109 (2025), p. 104828. ISSN: 2214-8604.

[17] Jesper Hesselvig and Rasmus T. Nygaard. "Studying SLS printing through multiphysics thermal and flow analysis with experimental validation." Bachelor's thesis. Aarhus University, 2024.

[18] J. D. Hoffman and J. J. Weeks. "Melting Process and the Equilibrium Melting Temperature of Polychlorotrifluoroethylene." In: *Journal of Research of the National Bureau of Standards, Section A: Physics and Chemistry* 66A.1 (1962), pp. 13–28. DOI: 10.6028/jres.066A.003.

[19] ISO. *DIN EN ISO 11357-4:2021 — Plastics — Differential scanning calorimetry (DSC) — Part 4: Determination of specific heat capacity*. Danish Standard version: DS/EN ISO 11357-4:2021. Geneva, Switzerland, 2021.

[20] ISO. *DS/EN ISO 11357-7:2022 — Plastics — Differential scanning calorimetry (DSC) — Part 7: Determination of crystallization and melting behaviour of polymer powders by DSC*. Danish Standard version: DS/EN ISO 11357-7:2022. Geneva, Switzerland, 2022.

[21] ISO. *DS/EN ISO 11357-1:2023 — Plastics — Differential scanning calorimetry (DSC) — Part 1: General principles*. Danish Standard version: DS/EN ISO 11357-1:2023. Geneva, Switzerland, 2023.

[22] Brent Stucker Mahyar Khorasani Ian Gibson David Rosen. *Additive Manufacturing Technologies*. 3rd. Springer Cham, 2020.

[23] Formlabs Inc. *Guide to Selective Laser Sintering (SLS) 3D Printing*. https://formlabs.com/blog/what-is-selective-laser-sintering/?srsltid=AfmBOor1nhqKft2A5fUrvg2Jcq72C4CcB4lKBTPVc Accessed: 2025-11-11. 2025.

[24] "Investigation of the mechanical, thermal, morphological and rheological properties of bio-based polyamide11/poly(lactic acid) blend reinforced with short carbon fiber." In: *Materials Today Communications* 30 (2022), p. 103030. ISSN: 2352-4928. DOI: https://doi.org/10.1016/j.mtcomm.2021.103030.

[25] Katalee Jariyavidyanont, Walter Focke, and René Androsch. "Thermal Properties of Biobased Polyamide 11." In: *Thermal Properties of Bio-based Polymers*. Ed. by Maria Laura Di Lorenzo and René Androsch. Cham: Springer International Publishing, 2019, pp. 143–187. ISBN: 978-3-030-39962-7. DOI: 10.1007/12_2019_47.

[26] Jr. Lauritzen John I. and John D. Hoffman. "Extension of theory of growth of chain-folded polymer crystals to large undercoolings." In: *Journal of Applied Physics* 44.10 (Oct. 1973), pp. 4340–4352. ISSN: 0021-8979. DOI: 10.1063/1.1661962.

[27] Chao Li, Scott E. Snarr, Erik R. Denlinger, Jeff E. Irwin, Michael F. Gouge, Pan Michaleris, and Joseph J. Beaman. "Experimental parameter identification for part-scale thermal modeling of selective laser sintering of PA12." In: *Additive Manufacturing* 48 (2021), p. 102362. ISSN: 2214-8604.

[28] Siyang Liu, Yingning Yu, Yi Cui, Hongfang Zhang, and Zhishen Mo. "Isothermal and non-isothermal crystallization kinetics of nylon-11." In: *Journal of Applied Polymer Science* 70.12 (1998), pp. 2371–2380. DOI: https://doi.org/10.1002/(SICI)1097-4628(19981219)70:12<2371::AID-APP9>3.0.CO;2-4.

[29] Laurence W. McKeen. "1 - Introduction to Plastics and Elastomers." In: *Effect of Temperature and other Factors on Plastics and Elastomers (Second Edition)*. Ed. by Laurence W. McKeen. Second Edition. Plastics Design Library. Norwich, NY: William Andrew Publishing, 2008, pp. 1–39. ISBN: 978-0-8155-1568-5.

[30] Mettler Toledo. *Differential Scanning Calorimetry - For Routine Analysis*. 2021.

[31] NETZSCH Analyzing & Testing. *PA11: Polyamide 11*. https://analyzing-testing.netzsch.com/en/polymers-netzsch-com/engineering-thermoplastics/pa11-polyamide-11. Accessed: 2025-12-02.

[32] K. Nakamura, K. Katayama, and T. Amano. "Some aspects of nonisothermal crystallization of polymers. II. Consideration of the isokinetic condition." In: *Journal of Applied Polymer Science* 17.4 (1973), pp. 1031–1041. DOI: https://doi.org/10.1002/app.1973.070170404.

[33] K. Nakamura, T. Watanabe, K. Katayama, and T. Amano. "Some aspects of nonisothermal crystallization of polymers. I. Relationship between crystallization temperature, crystallinity, and cooling conditions." In: *Journal of Applied Polymer Science* 16.5 (1972), pp. 1077–1091. DOI: https://doi.org/10.1002/app.1972.070160503.

[34] Celestino Padeste and Sonja Neuhaus. "Chapter 2 - Polymer-on-Polymer Structures Based on Radiation Grafting." In: *Polymer Micro- and Nanografting*. Ed. by Celestino Padeste and Sonja Neuhaus. Micro and Nano Technologies. Oxford: William Andrew Publishing, 2015, pp. 11–41. ISBN: 978-0-323-35322-9.

[35] Patrice Peyre, Yann Rouchausse, Denis Defauchy, and Gilles Régnier. "Experimental and numerical analysis of the selective laser sintering (SLS) of PA12 and PEKK semi-crystalline polymers." In: *Journal of Materials Processing Technology* 225 (2015), pp. 326–336. ISSN: 0924-0136. DOI: https://doi.org/10.1016/j.jmatprotec.2015.04.030.

[36] Natalie Rudolph. "Thermal Analysis and Rheology Methods." In: *Thermal Analysis and Rheology in Polymer Additive Manufacturing*. Version 1. Chapter 2. Selb, Germany: NETZSCH-Gerätebau GmbH, 2023, pp. 4–17.

[37] J. E. K. Schawe. "Influence of processing conditions on polymer crystallization measured by fast scanning DSC." In: *Journal of Thermal Analysis and Calorimetry* 116.3 (2014), pp. 1165–1173. DOI: 10.1007/s10973-013-3563-8.

[38] Jiho Seo, Anne M. Gohn, Olivia Dubin, Hideaki Takahashi, Hirokazu Hasegawa, Ruri Sato, Alicyn M. Rhoades, Richard P. Schaake, and Ralph H. Colby. "Isothermal crystallization of poly(ether ether ketone) with different molecular weights over a wide temperature range." In: *POLYMER CRYSTALLIZATION* 2.1 (2019), e10055. DOI: https://doi.org/10.1002/pcr2.10055.

[39] Jiho Seo, Xiaoshi Zhang, Richard P. Schaake, Alicyn M. Rhoades, and Ralph H. Colby. "Dual Nakamura model for primary and secondary crystallization applied to nonisothermal crystallization of poly(ether ether ketone)." In: *Polymer Engineering & Science* 61.10 (2021), pp. 2416–2426. DOI: https://doi.org/10.1002/pen.25767.

[40] Anshuman Shrivastava. "1 - Introduction to Plastics Engineering." In: *Introduction to Plastics Engineering*. Ed. by Anshuman Shrivastava. Plastics Design Library. William Andrew Publishing, 2018, pp. 1–16. ISBN: 978-0-323-39500-7.

[41] Sinterit. *Lisa X — sinterit.com*. https://sinterit.com/3dprinters/lisa-x/ [Accessed 18-04-2024]. 2024.

[42] Dominic Soldner, Sandra Greiner, Christian Burkhardt, Dietmar Drummer, Paul Steinmann, and Julia Mergheim. "Numerical and experimental investigation of the isothermal assumption in selective laser sintering of PA12." In: *Additive Manufacturing* 37 (2021), p. 101676. ISSN: 2214-8604. DOI: https://doi.org/10.1016/j.addma.2020.101676.

[43] Elias Spangsberg, Jesper Hesselvig, Rasmus Thoft Nygaard, Michal Kazimierz Budzik, and Michael Sandberg. "Multiscale Modelling of Heat Transfer in Selective Laser Sintering." Preprint, engrXiv. 2025. DOI: 10.31224/4704.

[44] Chris N. Velisaris and James C. Seferis. "Crystallization kinetics of polyetheretherketone (peek) matrices." In: *Polymer Engineering & Science* 26.22 (1986), pp. 1574–1581.

[45] Andong Wang, Caifeng Chen, Linchen Liao, Jilong Qian, Fuh-Gwo Yuan, and Ningyi Zhang. "Enhanced -Phase in Direct Ink Writing PVDF Thin Films by Intercalation of Graphene." In: *Journal of Inorganic and Organometallic Polymers and Materials* 30.5 (2020), pp. 1497–1502. DOI: 10.1007/s10904-019-01310-0.

[46] Yesong Wang, Feilong Li, Zixuan Sun, Chenyu Gu, Kunkun Fu, and Xiangming Zhao. "Effect of Fiber Content on the Preparation and Mechanical Properties of 3D Printed Short Carbon Fiber Reinforced PA Composites." In: *Polymers* 17.5 (2025). ISSN: 2073-4360. DOI: 10.3390/polym17050671.

[47] Feifei Yang, Navid Zobeiry, Ramulu Mamidala, and Xu Chen. "A review of aging, degradation, and reusability of PA12 powders in selective laser sintering additive manufacturing." In: *Materials Today Communications* 34 (2023), p. 105279. ISSN: 2352-4928. DOI: https://doi.org/10.1016/j.mtcomm.2022.105279.

[48] Sinterit Sp. z o.o. *Application of 3D printing in industry*. https://sinterit.com/3d-printing-guide/applications-of-3d-printing/application-of-3d-printing-in-industry/. Accessed: 2025-11-11. 2025.

[49] Sinterit Sp. z o.o. *PA11 CF – Carbon Fiber SLS Powder for Strong 3D Parts*. https://sinterit.com/materials/pa11-cf-carbon-fiber/. Accessed: 2025-11-11. 2025.

[50] Yunus A. Çengel and Afshin J. Ghajar. "Heat and Mass Transfer: Fundamentals & Applications." In: 5th. Includes derivation and forms of the general heat conduction equation in rectangular, cylindrical, and spherical coordinates, with and without heat generation. New York: McGraw-Hill Education, 2015. Chap. 2, pp. 79–82. ISBN: 978-0-07-339818-1.

A APPENDIX

This appendix contains the more detailed figures of results from the sintered cubes experiment. The figures are shown below:

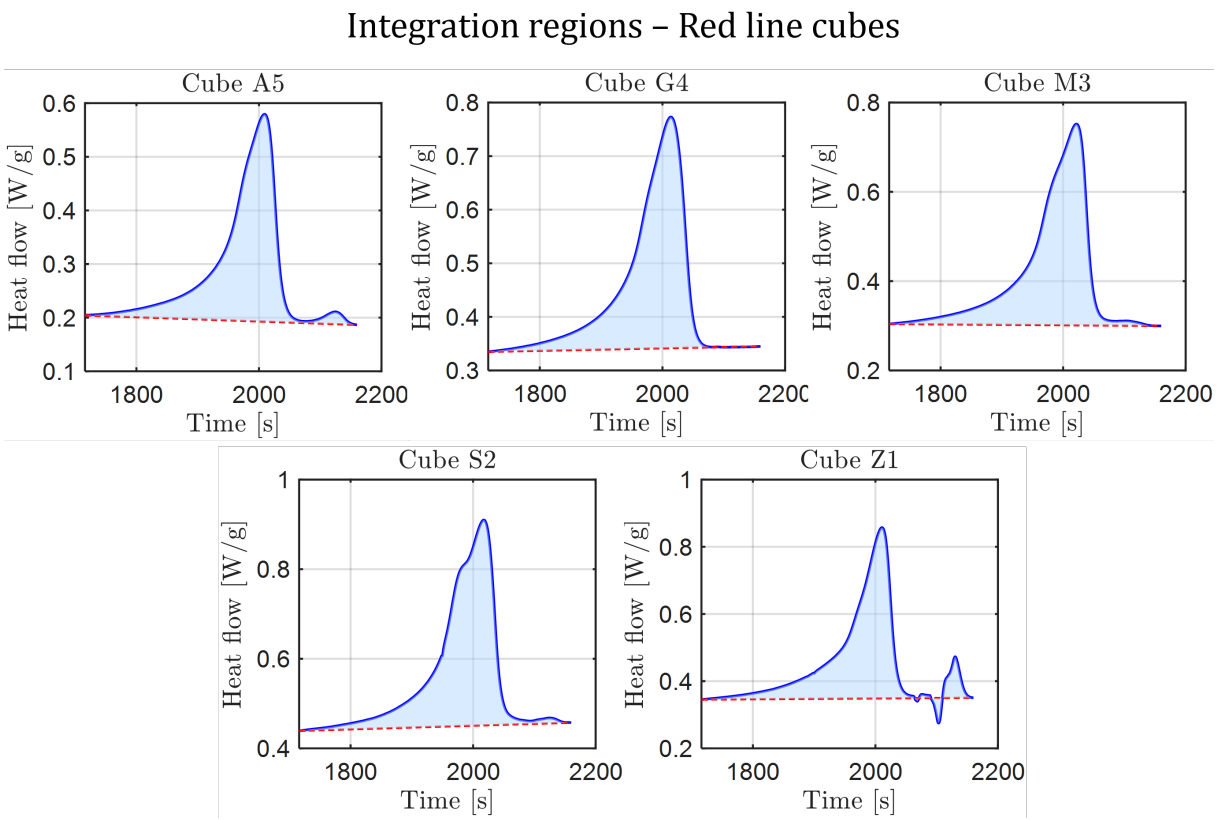

Figure A.1: Integration regions for the red-line cube positions (A5, G4, M3, S2, Z1, see. Figure 3.6). Each subplot shows the measured melting endotherm $\dot{Q}(t)$ (blue), the linear baseline used for integration (red dashed line), and the resulting shaded area corresponding to the latent heat of melting $\Delta H_{\infty,melt,2}$.

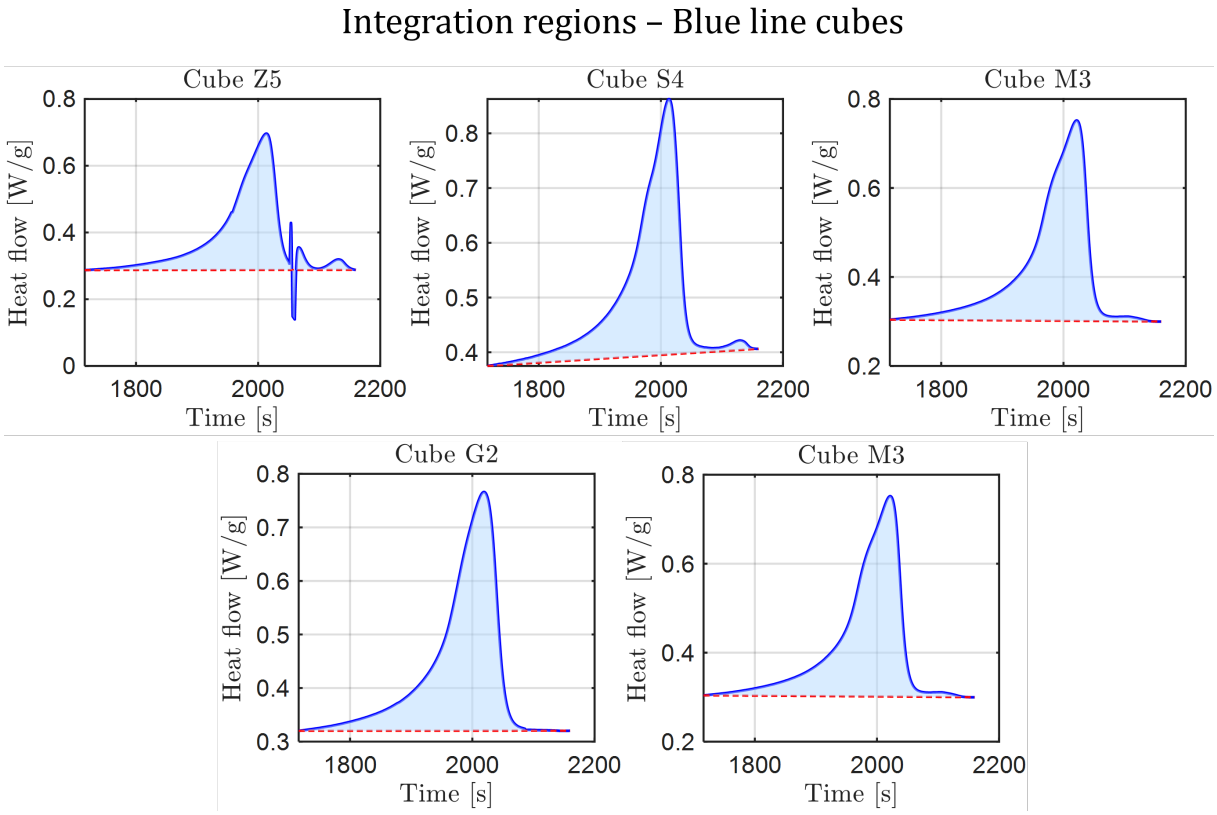

Figure A.2: Integration regions for the blue-line cube positions (Z5, S4, M3, G2, A1). As in Figure A.1, each subplot displays the melting heat-flow signal (blue), the constructed baseline (red dashed line), and the shaded integration area used to evaluate $\Delta H_{\infty,melt}$. These cubes represent the orthogonal "blue line" across the sample, again covering distances between $+98.8\,\mathrm{mm}$ and $-98.8\,\mathrm{mm}$ from the central M3 location.